Universiteit Utrecht

Master Thesis

Analysis of a stronger Atlantic Meridional Overturning Circulation in mid-Pliocene simulations

Author:
Julia Weiffenbach

Supervisors:
dr. Anna von der Heydt
dr. Michiel Baatsen

Institute for Marine and Atmospheric research Utrecht
Department of Physics
Utrecht University

April 15, 2021

Abstract

The mid-Pliocene is the most recent geological period with a greenhouse gas concentration of approximately 400 ppmv, similar to the present day. Proxy reconstructions indicate enhanced warming in the high North Atlantic in the mid-Pliocene, which has been suggested to be a response to a stronger Atlantic Meridional Overturning Circulation (AMOC). Ensemble results from the Pliocene Model Intercomparison Project Phase 2 (PlioMIP2) show a stronger AMOC and North Atlantic sea surface temperatures (SSTs) that match reconstructions better than PlioMIP1. A major difference between PlioMIP1 and PlioMIP2 is the closure of the Bering Strait and Canadian Archipelago in PlioMIP2. Previous studies have shown that closure of these Arctic gateways leads to an intensified AMOC due to altered freshwater fluxes in the Arctic.

For this study, we compared results from our Community Earth System Model (CESM1) simulations, using two pre-industrial runs with a CO_2 concentration of 280 and 560 ppmv and three mid-Pliocene runs with PlioMIP2 boundary conditions and a CO_2 concentration of 280, 400 and 560 ppmv. Our analysis shows that the simulated intensified AMOC in the mid-Pliocene is a result of the palaeogeographic boundary conditions, in particular the closure of the Arctic gateways. In the mid-Pliocene simulations, the AMOC intensifies by 2.6 - 4.2 Sv as a result of a higher salinity in the Labrador Sea. The stronger AMOC is accompanied by enhanced Atlantic northward ocean heat transport, which is the cause for amplified SST warming in the high North Atlantic in the mid-Pliocene. Further analysis on the variability of the AMOC suggests that the simulated mid-Pliocene AMOC shows fundamentally different behavior from the pre-industrial AMOC, where it appears that the mid-Pliocene AMOC is driven more strongly by salinity and has a weakened temperature feedback. This is supported a high sensitivity of the mid-Pliocene AMOC to the surface freshwater flux in the Labrador Sea.

Contents

Acknowledgements

I would like to start by thanking Anna von der Heydt and Michiel Baatsen for their guidance and support troughout the entire process of writing this thesis. Even though our meetings took place behind my somewhat uninspiring kitchen table, your interest and knowledge about the topic always managed to provide me with new insights and spark my curiosity. I really enjoyed our collaboration. I also want to extend my gratitude to Henk Dijkstra, whose valuable feedback helped in steering the direction of this thesis. Then I would also like to say thanks to Arthur Oldeman and André Jüling for helping me out when I got stuck on one of my many programming problems. I am very grateful for your help with these problems and the fact that you provided me with code that actually works.

Next, I want to thank Emma, Luke, Lena, Sophie, Handi, Ruben and Miriam for our study sessions and sometimes rather lengthy breaks. Being able to virtually study together has really helped to keep me on track during the whole process, as well as getting me started on some really good books. Also I would like to thank my friends and family for being there for me during these unusual times and always cheering me on. The virtual coffee breaks with the NRC crossword, walks around the neighborhood and video calls with opa en oma have kept me going. Last, I want to thank Sybren for always being there, although one might argue that that is less of a choice in these times, and reminding me that things always work out.

List of Abbreviations

AHT Atmospheric heat transport.

AMO Atlantic Multidecadal Oscillation.

AMOC Atlantic Meridional Overturning Circulation.

AOHT Atlantic ocean heat transport.

BS Bering Strait.

CAA Canadian Archipelago.

CCSM Community Climate System Model.

CESM Community Earth System Model.

DWF Deep water formation.

EOF Empirical orthogonal function.

GIS Greenland Ice Sheet.

IPOHT Indo-Pacific ocean heat transport.

KPP K-profile Parametrization.

MP Mid-Pliocene.

MSF Meridional streamfunction.

MTM Multi-Taper Method.

NA North Atlantic.

NH Northern Hemisphere.

OHT Ocean heat transport.

PC Principal component.

PI Pre-industrial.

PlioMIP Pliocene Model Intercomparison Project.

POP Parallel Ocean Program.

PRISM Pliocene Research, Interpretation and Synoptic Mapping.

SAT Surface air temperature.

SSS Sea surface salinity.

SST Sea surface temperature.

THT Total heat transport.

TOM Top-of-model.

1 Introduction

The mid-Pliocene (MP), roughly 3.3 - 3 million years ago, is the most recent geological period with a greenhouse gas concentration of approximately 400 ppmv, similar to the present day (Pagani et al., 2010). The MP is also the last geological period in which the average global temperature was higher than today, as shown in Figure 1, and that precedes the onset of the Northern Hemisphere glaciation and the glacial-interglacial cycles. The most important features of the MP climate are global surface temperatures that were $\sim 3°C$ higher than pre-industrial (PI) surface temperatures, ice sheets that were reduced in size, a reduced meridional temperature gradient and increased sea levels (Haywood et al., 2013, 2020). According to modelling studies, the MP is believed to be a geological analog for a future greenhouse climate (Burke et al., 2018) due to its CO_2 concentration close to present-day values and climate that is considered to be in equilibrium. Considering the fact that many MP boundary conditions, such as the geographic position of the continents and oceans, were very similar to the present day (Dowsett, 2007; Dowsett et al., 2016), studying components of the MP climate can provide us with knowledge that is highly relevant to understanding the effect of the current global warming on the Earth system, as well as the equilibrium warming under present-day CO_2 concentrations.

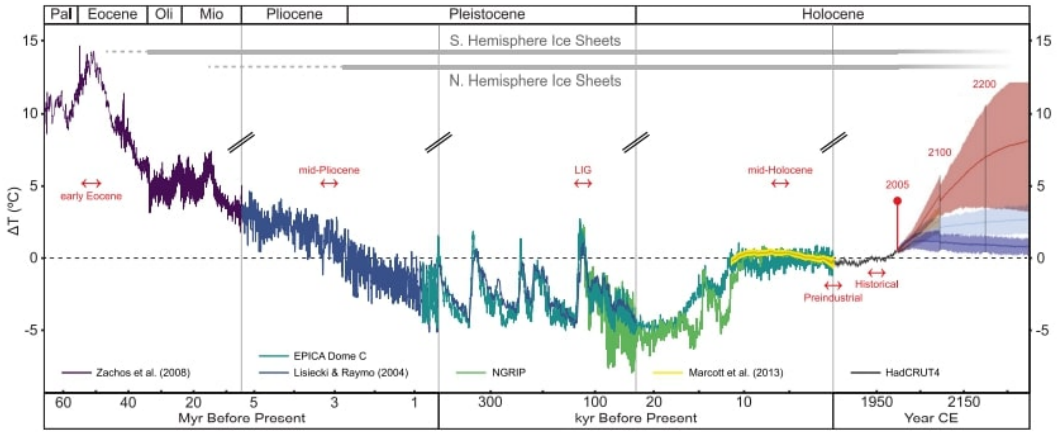

Figure 1: Global mean annual temperatures for the past 65 Ma relative to 1961-1990 global means. Reprinted from Burke et al. (2018).

One component of the climate system that is considered to have a major impact on the global climate is the Atlantic Meridional Overturning Circulation (AMOC). It has been linked to many other components of the climate system, such as average North Atlantic (NA) and Northern Hemisphere (NH) temperatures, precipitation and North Atlantic storm tracks (Jackson et al., 2015). The AMOC is the large-scale ocean circulation in the Atlantic Ocean that is driven by meridional density differences. It is associated with northward flow of warm, salty surface water that cools and becomes saltier due to evaporation during its flow northwards. This cooling and saltening increases the water density, eventually leading to sinking in the high North Atlantic, also known as North Atlantic Deep Water (NADW) formation. The NADW then moves southward at depths below approximately 1500 m. It eventually upwells in the Southern Ocean where it forms the warmer Antarctic Intermediate Water (AAIW) and moves northward again. This is the upper cell of the AMOC. There is also a weaker deep cell, which is associated with sinking

of very cold and salty Antarctic Bottom Water (AABW) that moves northward below depths of 4 km. After some time, it will rise and mix with the southward flowing NADW.

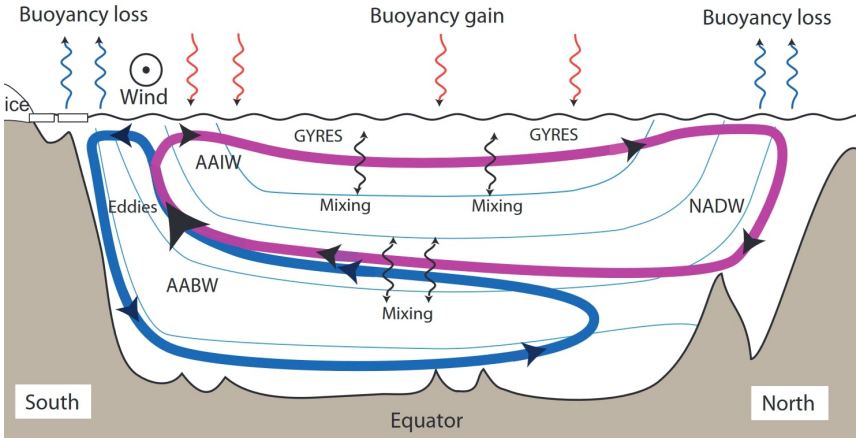

Figure 2: Schematic representation of the AMOC reprinted from Vallis (2017) showing several processes involved in the AMOC: mixing, surface buoyancy fluxes, eddies and wind stress.

There are several important processes involved in the AMOC: mixing, surface buoyancy fluxes, eddies and wind stress, as is shown in the schematic representation of the AMOC in Figure 2. Classical scaling, which assumes geostrophic balance and advective-diffusive balance over the thermocline, shows that a meridional density gradient $\Delta\rho$ is responsible for meridional overturning (Vallis, 2017). The strength of the meridional transport Ψ_m can then be related to $\Delta\rho$ and the vertical diffusivity κ_v by

$$\Psi_m \sim \kappa_v^{2/3} \Delta\rho^{1/3} \tag{1.1}$$

As the AMOC is driven by meridional density differences, it responds strongly to freshwater anomalies in the high NA. Thornalley et al. (2018) recently showed that at the end of the Little Ice Age (approximately 1850 AD), enhanced freshwater flux from the Arctic and Nordic seas weakened convection in the Labrador Sea as well as the AMOC itself. This is in agreement with the work of Delworth and Zeng (2012), who found that a strengthened AMOC is associated with positive density anomalies over regions of deep water formation (DWF), where salinity anomalies dominate the density anomalies. It is also suggested that temperature-induced density variations are a response to AMOC changes, rather than a driver. This is consistent with the existence of a sea surface temperature (SST) fingerprint of the AMOC: a strengthened AMOC corresponds to warming in the subpolar gyre region due to increased northward ocean heat transport (OHT) and cooling in the Gulf Stream region due to the Gulf Stream shifting southwards as a response to a stronger deep western boundary current (Caesar et al., 2018). Observations and models show a "warming hole" in the high-latitude NA southeast of Greenland as a response to anthropogenic climate change, which has been linked to a weakening AMOC and its associated northward OHT (Drijfhout et al., 2012). This indicates that an intensified AMOC will lead to enhanced warming in this location by transporting more heat to high latitudes. Proxy data from the MP shows that enhanced warming in the high NA can be reconstructed for that time period (Dowsett et al., 2013). Marine proxy data (Raymo et al., 1996; Ravelo and Andreasen, 2000; Frenz et al., 2006) indeed suggests that this warming is a result of a stronger AMOC in the MP.

Initiated in 2008, the Pliocene Model Intercomparison Project Phase 1 (PlioMIP1) was the first time that a coordinated model ensemble of global circulation models was run for the MP. Its goal was to analyze model results and sample their structural uncertainty for a 300k year interval (3.264 to 3.025Ma) in the MP, for which reconstructed temperature data sets are available (Haywood et al., 2010, 2011). One of its main results was that the models were able to reproduce many characteristics of sea surface temperature (SST) and surface air temperature (SAT), but could not consistently reproduce the magnitude of warming that is expected at high latitudes (Dowsett et al., 2013; Haywood et al., 2020). This includes the reconstructed enhanced warming in the high NA, which has been linked to a stronger AMOC during the MP (Raymo et al., 1996; Frenz et al., 2006). Only five out of eight ensemble models simulated a stronger AMOC during the MP, while the models that simulated a weaker AMOC during the MP still showed enhanced warming in the high-latitude NA (Zhang et al., 2013). This would indicate that a stronger AMOC is not responsible for enhanced warming in the NA in the PlioMIP1 simulations.

Based on the results of PlioMIP1, PlioMIP Phase 2 (PlioMIP2) was initiated. PlioMIP2 is an ensemble of fifteen coupled atmosphere-ocean ESMs that all utilize the same MP boundary conditions and have at least one MP and one PI simulation (Haywood et al., 2016). Its goal was to reduce the uncertainty in the boundary conditions and in proxy reconstructions by increasing the temporal resolution (Haywood et al., 2016). To achieve this, a time slice was chosen on an interglacial peak (3.205 Ma) with an orbital forcing similar to the present day. In addition, boundary conditions such as palaeogeography and ice sheet cover were provided based on an updated reconstruction by the Pliocene Research, Interpretation and Synoptic Mapping (PRISM4) project (Dowsett et al., 2016). The main differences between these boundary conditions and those used in PlioMIP1 include the closure of the Bering Strait (BS) and Canadian Archipelago (CAA) as well as a strong reduction in the extent of the Greenland Ice Sheet (GIS).

The closure of the Arctic gateways in the PlioMIP2 MP simulations is expected to have a large effect of the MP AMOC strength. In a study by Otto-Bliesner et al. (2017) of their PlioMIP1 model it was shown that closure of the BS and CAA significantly strengthens the AMOC due to the decrease in freshwater transport from the Pacific Ocean into the Arctic Ocean. This led to reduced freshwater transport through the Fram Strait into the NA, increasing salinity in the high NA and thereby stimulating deep water formation. In the PRISM4 reconstruction (Dowsett et al., 2016) it is suggested that the closure of these Arctic gateways may lead to a strengthened AMOC, concurrent with increased northward OHT that drives the enhanced high NA warming as indicated by proxy data. This is supported by the analysis of the large-scale features of the PlioMIP2 ensemble results (Haywood et al., 2020) where it appears that the BS and CAA closure may have been a main contributor to the better match between proxy reconstructed and PlioMIP2 ensemble NA SSTs.

The PlioMIP2 ensemble data analysis published by Zhang et al. (2021) shows that all PlioMIP2 models simulate a stronger AMOC and warming in the NA SSTs, as can be seen in Figure 3(a). Nevertheless, the multi-model mean NA SST warming simulated by the PlioMIP2 ensemble is still less than reconstructed using proxy data, as illustrated in the difference between Figure 3(c) and 3(d). That being said, PlioMIP2 NA SSTs do match the reconstructions better than the PlioMIP1 ensemble (Dowsett et al., 2013).

In Figure 3(a) and 3(b) we observe a large spread in the PlioMIP2 data. For instance, the response of the North Atlantic OHT is inconsistent across the ensemble: there appears to be minimal correlation between the NA SST warming and OHT in Figure 3(b). The model from Utrecht University, referred to as CCSM4-Utrecht in PlioMIP2, simulates one of the highest SST anomalies of the ensemble yet its OHT anomaly is at the median value. In fact, a similar NA SST anomaly can correspond to either negative or positive OHT anomalies depending on the model. Therefore, while all models simulate a stronger AMOC, they do not all find concurrent positive OHT anomalies. The NA SST warming also does not significantly correlate with either the AMOC strength or OHT. Overall, the analysis by Zhang et al. (2021) does not find a consistent relationship between the OHT, NA SSTs and AMOC strength in the PlioMIP2 ensemble.

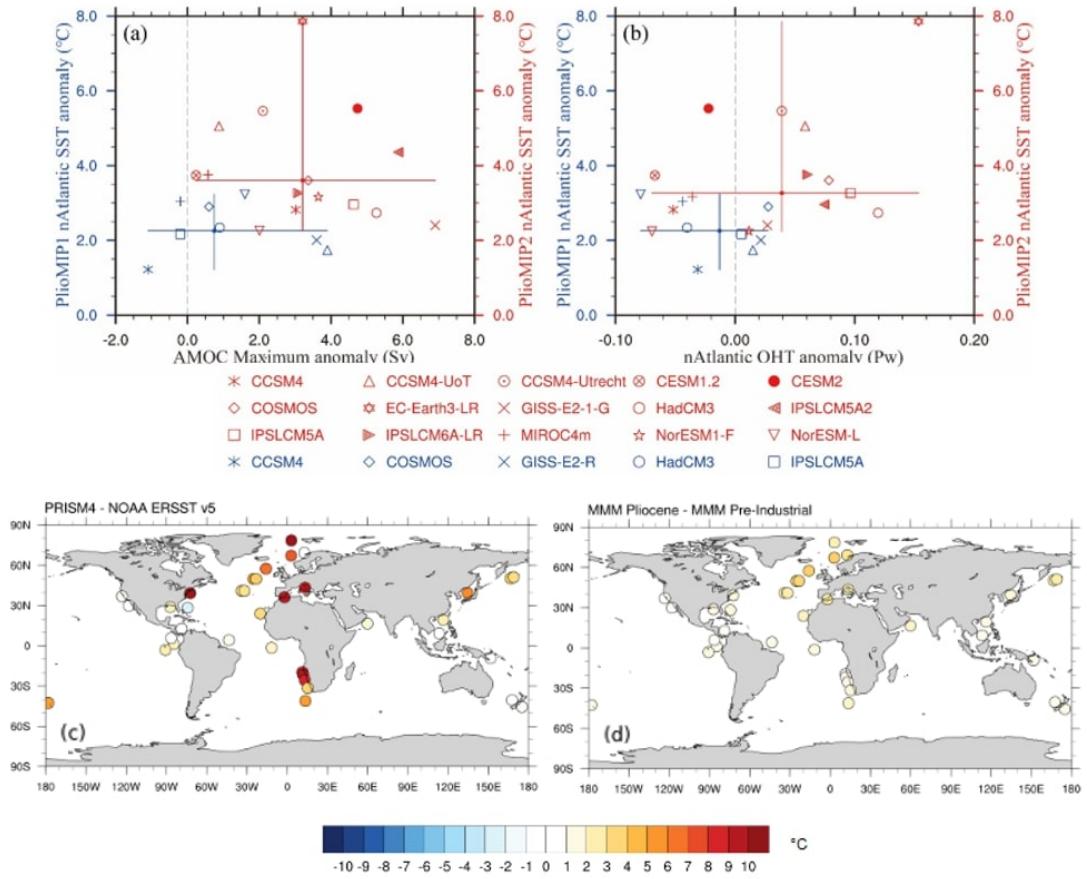

Figure 3: (a): PlioMIP1 (blue) and PlioMIP2 (red) ensemble results comparing the simulated AMOC maximum and the high-latitude NA SST anomalies. (b): PlioMIP1 (blue) and PlioMIP2 (red) ensemble results comparing the simulated high-latitude NA SST and the NA OHT anomalies. The NA OHT and SST is the average value between 30°N and 80°N. Anomalies are with respect to the PI simulations. Each symbol represents an ensemble model and the horizontal and vertical lines show the spread of ensemble results, where their intersection indicates the median value. (c): MP-PI SST anomaly at indicated sites, reconstructed with PRISM4 - NOAA ERSSTv5. (d): PlioMIP2 multi-model mean (MMM) MP-PI SST anomaly at indicated sites. Adapted from Zhang et al. (2021) and Haywood et al. (2020).

The inconsistent response of the OHT and NA SST warming to a stronger AMOC in the PlioMIP2 ensemble and the prospect that the closure of the Arctic gateways has a significant effect on the MP AMOC calls for further investigation to see what processes are taking place at an individual model level. As mentioned earlier, while CCSM4-Utrecht shows an OHT anomaly at the median ensemble value and an AMOC strength anomaly below the median, its NA SST anomaly is one of the highest in the ensemble. We are interested to see what is driving the processes that produce this individual CCSM4-Utrecht model result. In this thesis, the MP and PI CCSM4-Utrecht simulations will be analyzed, supplemented with the analysis of two MP and one PI simulation with different CO_2 concentrations. We will aim to answer the following research questions:

- **What drives the stronger AMOC in the mid-Pliocene CCSM4-Utrecht simulation?**
- **Can the stronger AMOC explain the amplified warming of North Atlantic SSTs in the mid-Pliocene simulation?**
- **What is the difference in AMOC and SST variability between the mid-Pliocene and pre-industrial simulations and can we explain this possible difference?**

By answering these questions, we aim to provide further insight into the behavior of the mid-Pliocene AMOC and the impact of mid-Pliocene boundary conditions on the North Atlantic region in CCSM4-Utrecht. The thesis is structured as follows: we will first given an overview of the CCSM4-Utrecht model setup and model analysis in chapter 2. Chapter 3 will show the results of the analysis, of which a discussion will follow in chapter 4. Finally, we will conclude with chapter 5 where we will answer the research questions.

2 Methods

2.1 Model description

The simulations analyzed for this thesis are performed with the Community Earth System Model (CESM, version 1.0.5.) (Hurrell et al., 2013). CESM 1.0.5. is a fully coupled climate model consisting of four separate models that simulate the atmosphere, ocean, land surface and sea-ice that are coupled through a central coupler. The ocean is modeled by the Parallel Ocean Program (POP2) on a displaced pole grid with a resolution of 0.27–0.54^o×1.1^o and 60 vertical levels. The sea-ice component is modelled by the Community Ice CodE (CICE4) on the same horizontal grid as POP2. The atmosphere is modelled by the Community Atmosphere Model (CAM4) on a horizontal grid resolution of 2.5^o×1.9^o and has 27 vertical levels. The land component is modelled by the Community Land Model (CLM4) on the same horizontal grid as CAM4. The setup we use here is equivalent to version 4 of its predecessor: the Community Climate System Model 4 (CCSM4). Following the PlioMIP2 convention, we from here on refer to our simulations as CCSM4-Utrecht. For further details and documentation of CCSM4, the reader is referred to the documentation provided by the National Center for Atmospheric Research (https://www.cesm.ucar.edu/models/ccsm4.0/).

2.1.1 Ocean vertical mixing parametrization

All CCSM4-Utrecht simulations utilize the nonlocal K-profile parametrization (KPP) scheme of Large et al. (1994), as described in the POP2 Reference Manual (Smith et al., 2010). This KPP scheme includes vertical diffusivity κ_B in the oceanic boundary layer h and vertical diffusivity κ_{IN} below the boundary layer $z > h$, where κ_{IN} includes a superposition of four processes:

$$\kappa_{IN} = \kappa_w + \kappa_s + \kappa_c + \kappa_d \tag{2.1}$$

Here, κ_w represents the background diffusivity, κ_s shear instability mixing, κ_c convective instability and κ_d double diffusion. The background diffusivity κ_w varies in the vertical direction z and is given by

$$\kappa_w = vdc1 + vdc2 \tan^{-1}\left((z - D)L_{inv}\right) \tag{2.2}$$

where $vdc1$ is the background diffusivity at depth D, $vdc2$ is the variation amplitude and L_{inv} is the inverse depth scale of the transition region.

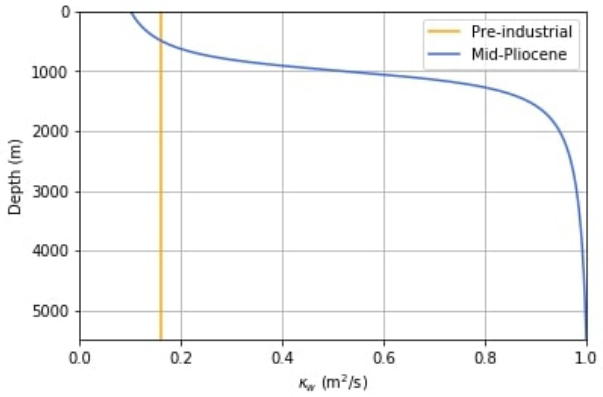

Figure 4: Vertical profiles of the background diffusivity κ_w in the PI and MP simulations.

The background vertical diffusivity κ_w is of interest because it is defined differently in the MP and the PI CCSM4-Utrecht simulations. The standard for the background vertical diffusivity in the POP2 KPP scheme is a background value of $\kappa_w = 0.17$ cm^2/s that is homogeneous in the vertical direction. κ_w does vary in the horizontal direction in this standard case with an enhanced κ_w in two bands at 29.8^{o}N/S and the Banda Sea as well as a reduced κ_w near the equator. In addition, the standard scheme includes a tidal and overflow mixing parametrization to more accurately model locally enhanced mixing caused by these processes. As there is no information on locally enhanced mixing in the MP, all horizontal variations and the tidal and overflow parametrizations are turned off for the MP simulations. Instead, the MP vertical mixing scheme was altered to contain a background κ_w that is homogeneous in the horizontal direction and increases in the vertical direction: $vdc1 = 0.524$ cm^2/s, $vdc2 = 0.313$ cm^2/s, $D = 1000$ m and $L_{inv} = 4.5e\text{-}3$ m^{-1}. While we described the standard mixing parametrization earlier, this scheme was also not utilized in the PI simulations. In the PI simulations, the horizontal variations and the tidal and overflow parametrizations are also turned off. There, the resulting κ_w is homogeneous in both horizontal and vertical direction as $vdc1 = 0.16$ cm^2/s and $vdc2 = 0$ cm^2/s. The resulting PI and MP background mixing coefficients are both homogeneous in the horizontal direction and their κ_w profile in the vertical direction is shown in Figure 4.

Jayne (2009) and Jochum (2009) have previously shown that the North Atlantic region is sensitive to variations in the magnitude of the vertical mixing coefficient in CCSM3. However, Jochum (2009) found that latitudinal variations in the background vertical diffusivity have no effect on the AMOC strength. Therefore, we do not expect that the absence of horizontal variations in the background vertical diffusivity of the CCSM4-Utrecht PI and MP simulations will significantly impact the AMOC strength. In addition, as latitudinal variations in background vertical diffusivity are absent in both the PI and MP CCSM4-Utrecht simulations, this feature does not compromise their comparison. Jayne (2009) does find that stronger abyssal mixing has a notable effect on the deep meridional overturning but no significant effect is observed on the upper AMOC cell nor on the meridional ocean heat transport. As the MP simulations have a weaker κ_w above 1000 m depth and a stronger κ_w below 1000 m depth compared to the PI simulations, some effect on the AMOC cell and ocean temperature and salinity in the North Atlantic is to be anticipated. Even so, based on these earlier studies we do not expect that this will have a large impact on the simulated AMOC strength or the meridional ocean heat transport. In Appendix A, the possible effect of the different background vertical mixing coefficients in the PI and MP simulations is discussed and analyzed further.

2.2 Experimental setup

In the experimental setup for PlioMIP2, Haywood et al. (2016) proposed two core experiments: a PI simulation with 280 ppmv CO_2, denoted by E^{280}, and a MP simulation with 400 ppmv CO_2, denoted by Eoi^{400}. This follows the nomenclature Ex^c where c is the CO_2 concentration in ppmv and x are the MP boundary conditions as opposed to the PI boundary conditions. Therefore, x can be none, meaning that the PI boundary conditions apply, or either or both o and i, which are MP orography and ice sheets, respectively. The orography also includes the land-sea mask, bathymetry, vegetation, soils and lakes.

In addition to the two core experiments E^{280} and Eoi^{400} that were proposed, the CCSM4-Utrecht simulations also include the runs E^{560}, Eoi^{280} and Eoi^{560}, as shown in Figure 5. These runs will

allow for separate analysis of the CO_2 forcing and the forcing by prescribed MP boundary conditions. E^{280} and Eoi^{400} are the initial simulations that include a longer spin-up phase. E^{560} is initialized from core experiment E^{280} after 3000 years while Eoi^{280} and Eoi^{560} are initialized from core experiment Eoi^{400} after 2000 years.

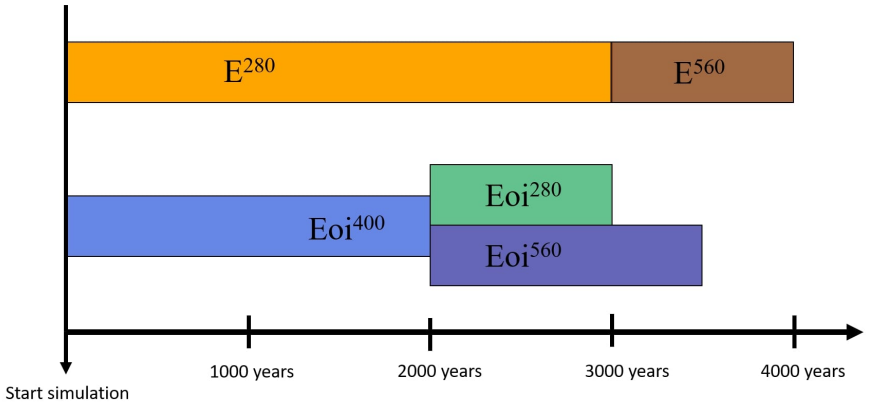

Figure 5: Overview of the analyzed CCSM4-Utrecht simulations and their runtime.

2.2.1 PlioMIP2 boundary conditions

The MP CCSM4-Utrecht simulations required implementing the updated PRISM4 paelaeogeography reconstruction (Dowsett et al., 2016) by prescribing the MP topography and bathymetry as an anomaly to the PI geography (Haywood et al., 2016). The PRISM4 reconstruction is shown in Figure 6 and includes the closure of the Bering Strait and Canadian Archipelago in the MP, as well as some modifications to other seaways.

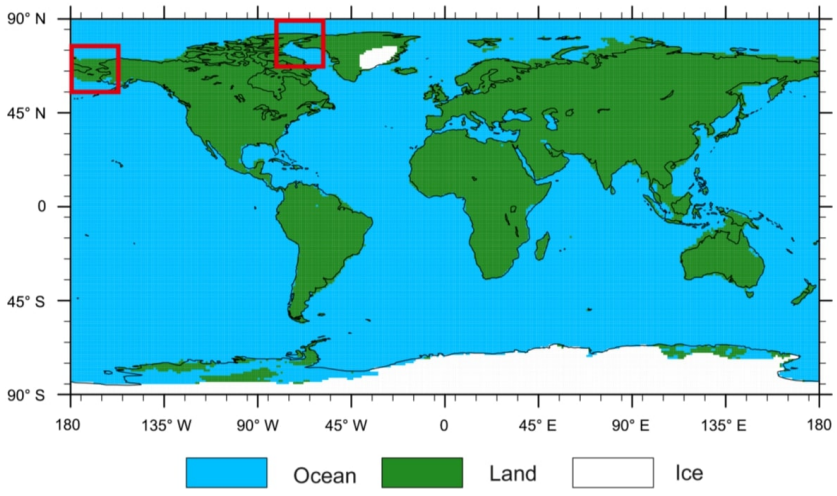

Figure 6: The palaeogeographic PRISM4 land-sea mask including ice sheets. The black contours indicate the present-day coastlines. Red boxes show the closure of the Bering Strait and Canadian Archipelago in the PRISM4 land-sea mask. Reprinted from Haywood et al. (2016).

The PRISM4 reconstruction also includes a drastically reduced ice sheet on Greenland, where ice is only present in the East Greenland Mountains, based on the results of the Pliocene Ice

Sheet Modelling Project (PLISMIP) (Koenig et al., 2015; Dolan et al., 2015). As Figure 6 shows, West Antarctica is also significantly different in the MP compared to the PI due to raised sea levels and the lack of ice cover. This reconstruction is based on ice core data and modelling (Naish et al., 2009; Pollard and DeConto, 2009). For East Antarctica, the earlier PRISM3D ice sheet reconstruction (Dowsett et al., 2010) is used because it is still the most consistent with available data. The PRISM4 reconstruction also includes vegetation, which remains the same as in PlioMIP1 (Haywood et al., 2010, 2011), and new lake and soil distributions (Pound et al., 2014).

2.3 Data analysis

For all simulations, yearly data of the last 200 model years is analyzed. Average fields are also computed over this 200 year interval. We have chosen this interval length because it is long enough to be representative for the mean state and variability in observed variables but also excludes the majority of spin-up effects that may be present in earlier model years. The applied boundaries for the different ocean regions are shown in Figure 7, where the Labrador Sea is separately indicated by the red boundary. The red line in Figure 7 indicates the 40°N latitude at which the AMOC strength and Atlantic ocean heat transport (AOHT) strength is defined, as further described in the following subsections.

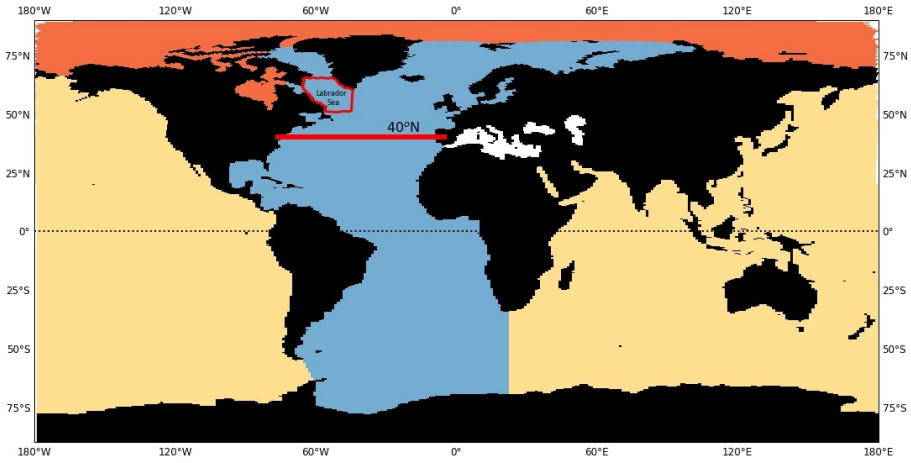

Figure 7: Ocean regions in CCSM4-Utrecht where blue indicates the Atlantic Ocean, orange the Arctic Ocean, yellow the Indian and Pacific (Indo-Pacific) Ocean and white the Mediterranean, Black and Caspian Sea. The red line shows the latitude 40°N where the AMOC and AOHT strength are computed. The red contour in the high NA shows the Labrador Sea region.

2.3.1 AMOC and AMO

The AMOC will be analyzed using the meridional streamfunction (MSF, Ψ). The Atlantic MSF is defined at each latitude y and depth z as

$$\Psi = \int_0^z \int_{x_W}^{x_E} v \, dx \, dz \tag{2.3}$$

where $z = 0$ at the sea surface and increases with depth, v is the meridional velocity of each grid cell of dx in longitude and dz in depth, and $x_W(z)$ and $x_E(z)$ are the positions of the westward

and eastward boundaries of the Atlantic basin. Figure 7 shows the Atlantic basin region of the CCSM4-Utrecht model in blue.

To consistently analyze the AMOC for each simulation, we will define the AMOC strength as the maximum of the MSF at 40°N below a depth of 500 m: $\Psi_{\max}(y = 40°\text{N}, z > 500 \text{ m})$. The minimum depth is set at 500 m to exclude the shallow wind-driven gyre cells. The selected latitude of 40°N is based on several considerations. The first is the location of the AMOC maximum, which is on average between 35°N-40°N in the analyzed PI and MP simulations. Secondly, we strive to uncover whether there is a relationship between high NA SST warming and the AMOC strength. The high NA SST warming is located between approximately 45-60°N which makes 40°N a logical choice for observing the simulated AMOC strength and its associated heat transport.

As we are interested in possible changes in SST and AMOC variability between the simulations, we will also consider the Atlantic Multidecadal Oscillation (AMO) in our analysis. The AMO, also known as the Atlantic Multidecadal Variability (AMV), is an internal mode of multidecadal variability in North Atlantic SSTs that is related to the AMOC. Its pattern has been identified by Kushnir (1994) as a negative SST anomaly off the coast of Newfoundland and a positive SST anomaly over the rest of the North Atlantic (von der Heydt et al., 2020). There are several mechanisms that have been proposed to be responsible for the AMO, including westward propagation of subsurface temperature anomalies in the NA, atmospheric forcing and Atlantic-Arctic exchange processes (Frankcombe et al., 2010). While we will not look at these processes in detail for this study, we want to be able to identify variability in our simulations as being related to the AMO. For this we will use the AMO index, defined as the North Atlantic SST anomaly between 0-80°W and 0-60°N.

2.3.2 Meridional heat transport

To account for the warmer MP NA SSTs, we expect to find enhanced northward ocean heat transport in the Atlantic as a consequence of the intensified AMOC. Classical scaling shows that the ocean heat transport of an overturning cell (OHT_{ov}) is linearly proportional to the strength of the overturning Ψ_m and the temperature difference between the northward and southward flowing water in the cell ΔT (Vallis and Farneti, 2009):

$$OHT_{ov} \propto \Psi_m \Delta T \tag{2.4}$$

To define the global ocean heat transport (OHT) we may assume that in a steady climate, mesoscale eddies and dissipation can be neglected to approximate the total meridional OHT at each latitude y as the Eulerian mean circulation (Yang et al., 2015):

$$OHT = \rho_0 c_p \int\int vT \, dx \, dz \tag{2.5}$$

Here, v represents the meridional velocity and T the ocean potential temperature of each grid cell of dx in longitude and dz in depth. The constants ρ_0 and c_p are the average density and specific heat of sea water, respectively. For this study, we compute ocean meridional heat transport using the yearly mean $\overline{vT}$, where the overbar represents the yearly mean field:

$$OHT = \rho_0 c_p \int\int \overline{vT} \, dx \, dz \tag{2.6}$$

This yearly OHT can be partitioned into a mean flow $\overline{\text{OHT}}$ and a transient eddy component OHT' (Viebahn et al., 2016) using $v = \overline{v} + v'$ and $T = \overline{T} + T'$ where $\overline{v}$ and $\overline{T}$ are the yearly mean and v' and T' the eddy components of the respective v and T fields:

$$OHT = \overline{OHT} + OHT' \tag{2.7}$$

Here, the time mean component $\overline{\text{OHT}}$ is

$$\overline{OHT} = \rho_0 c_p \int \int \overline{v}\overline{T}\, dx\, dz \tag{2.8}$$

and the transient eddy component OHT' is

$$OHT' = \rho_0 c_p \int \int \overline{v'T'}\, dx\, dz = OHT - \overline{OHT} \tag{2.9}$$

As our focus is on the Atlantic Ocean, analysis will be largely done on the Atlantic ocean heat transport (AOHT). We find the AOHT in the same manner as the global OHT from equation 2.6, but now integrating between the longitudinal boundaries x_E and x_W of the Atlantic basin. The temporal decomposition into a time mean and transient eddy component is then performed in the same manner as for the global OHT:

$$AOHT = \rho_0 c_p \int \int_{x_W}^{x_E} \overline{vT}\, dx\, dz = \overline{AOHT} + AOHT' \tag{2.10}$$

To be able to determine the effect of a changing AMOC on the AOHT associated with overturning, the time mean $\overline{\text{AOHT}}$ is separated into a zonal mean overturning component and an azonal gyre component. This will approximately separate $\overline{\text{AOHT}}$ in heat transport that can be attributed to the overturning circulation and heat transport that results from barotropic gyre circulation. Following Dijkstra (2007) and Viebahn et al. (2016), we find that:

$$\overline{AOHT} = \overline{AOHT}_{ov} + \overline{AOHT}_{az} \tag{2.11}$$

where

$$\overline{AOHT}_{ov} = \rho_0 c_p \int \int_{x_W}^{x_E} \langle\overline{v}\rangle\langle\overline{T}\rangle\, dx\, dz \tag{2.12}$$

$$\overline{AOHT}_{az} = \rho_0 c_p \int \int_{x_W}^{x_E} \langle\overline{v}^*\overline{T}^*\rangle\, dx\, dz \tag{2.13}$$

Here, $\langle\overline{v}\rangle$ and $\langle\overline{T}\rangle$ are the zonal mean of $\overline{v}$ and $\overline{T}$ at each latitude, and $\overline{v}^*$ and $\overline{T}^*$ are the azonal components such that $\overline{v} = \langle\overline{v}\rangle + \overline{v}^*$ and $\overline{T} = \langle\overline{T}\rangle + \overline{T}^*$.

This separation into overturning and azonal components can only be done for the time mean component. Therefore, the total AOHT will always contain an eddy component in addition to the mean overturning and azonal components:

$$AOHT = \overline{AOHT}_{ov} + \overline{AOHT}_{az} + AOHT' \tag{2.14}$$

The variability contained in the eddy component is primarily a result of the seasonal cycle and is therefore largely unaffected by the choice of averaging period (Viebahn et al., 2016). Especially in areas with high eddy activity, such as the Southern Ocean, the eddy component is significant.

At 40°N, the mean contribution of the eddy term is small: 0.03 PW on a total AOHT of 0.48 PW in E[280]. The eddy term has a comparable magnitude and standard deviation in all PI and MP simulations. Hence, we are able to neglect the eddy contribution and define the strength of the AOHT and its components at this latitude. This allows us to obtain an accurate picture of the behavior of overturning and azonal AOHT with minimal error contained in the eddy component.

To gain a complete picture of the meridional heat transport in the simulations, meridional atmospheric heat transport (AHT) must also be taken into account. The AHT is defined as the difference between the top-of-model total heat transport (TOM THT) and computed OHT at each latitude: $AHT = THT_{TOM} - OHT$. The TOM THT at each latitude y is computed using the net incoming and outgoing radiative fluxes F_{net} at the TOM, integrating over all longitudes and from the South Pole up to y:

$$THT_{TOM} = \int_{90^{\circ}\text{S}}^{y} \int_{180^{\circ}\text{W}}^{180^{\circ}\text{E}} F_{\text{net}} \, dx \, dy \tag{2.15}$$

3 Results

3.1 Strengthened mid-Pliocene AMOC

The CCSM4-Utrecht E^{280} simulates an average AMOC strength of 17.9 Sv at 26.5°N, which is within the range of the observed AMOC strength at 26.5°N by Kanzow et al. (2010) of 18.7 ± 2.1 Sv. As we have defined the AMOC strength at 40°N, the average E^{280} AMOC strength is 18.6 Sv. The simulated MP Eoi^{400} AMOC strength at 40°N is 21.8 Sv, which is +3.2 Sv from the E^{280} AMOC. Figure 8(a) shows the Atlantic MSF of E^{280} as well as the difference between the Eoi^{400} and E^{280} Atlantic MSF in Figure 8(b). There we find that the increase in AMOC strength in the MP Eoi^{400} simulation is concurrent with strengthening and deepening of the AMOC cell.

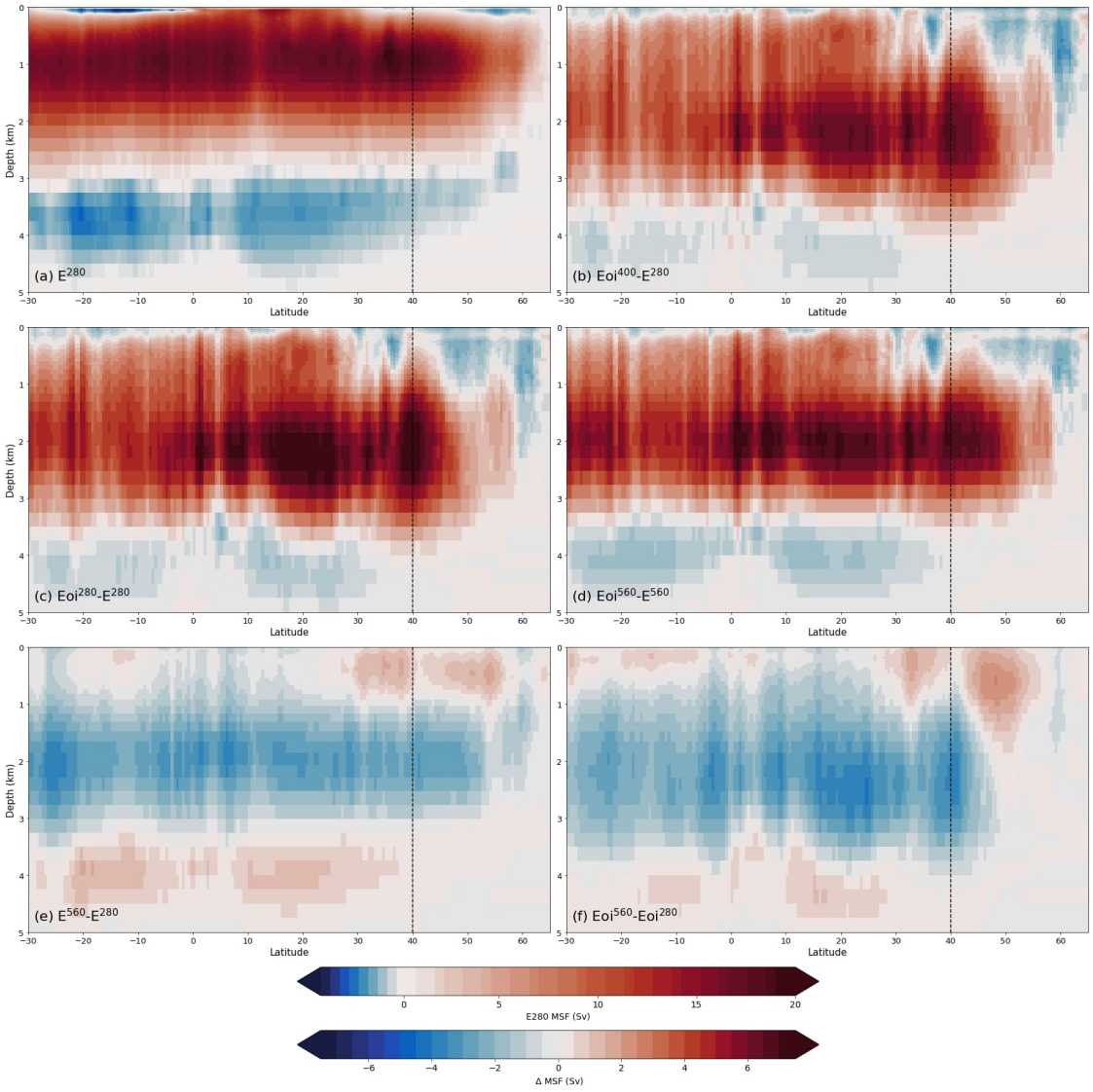

Figure 8: (a): Average simulated E^{280} Atlantic MSF. (b) - (f): Aaverage simulated differences in Atlantic MSF (Δ MSF) between (b) Eoi^{400}-E^{280}, (c) Eoi^{280}-E^{280}, (d) Eoi^{560}-E^{560}, (e) E^{560}-E^{280} and (f) Eoi^{560}-Eoi^{280}. Vertical dashed lines indicate 40°N latitude at which the AMOC strength is determined.

The difference between the other simulations and the PI E^{280} are: -0.24 Sv for E^{560}, +4.2 Sv for Eoi^{280} and +2.6 Sv for Eoi^{560}. Therefore, all MP simulations simulate a stronger AMOC. Figures 8(c) - (f) allow for further investigation into the cause of this strengthening AMOC in the MP simulations: Figure 8(c) and 8(d) show the effect of MP boundary condition at different CO_2 concentrations while Figure 8(e) and 8(f) show the effect of doubling the CO_2 concentration in both the PI and MP. The figures indicate that the strengthening and deepening of the AMOC in all MP simulations is a response to the boundary conditions rather than CO_2 increase. The pattern of strengthening and deepening in the Atlantic MSF as a response to MP boundary conditions in Figure 8(c) and 8(d) is very similar to that of Eoi^{400}-E^{280} (Figure 8(b)). The MP boundary conditions' effect on the AMOC strength is significant: the AMOC strength at 40°N is 34% stronger in Eoi^{280} than in E^{280} and 14% stronger in Eoi^{560} than in E^{560}. At the same time we observe that doubling of the CO_2 concentration actually induces some weakening and shallowing of the AMOC cell in both the PI and MP. The effect of doubling the CO_2 concentration on the AMOC strength is relatively smaller, especially in the PI simulations. There, the AMOC strength is 1.3% weaker in E^{560} than in E^{280}. In Eoi^{560}, the AMOC strength is 6.9% weaker than in Eoi^{280} with a similar pattern of weakening and shallowing in the Atlantic MSF in Figure 8(f) that we saw for E^{560}-E^{280} (Figure 8(e)). Clearly, the MP boundary conditions lead to strengthening of the AMOC.

3.2 North Atlantic salinity and freshwater exchange

In Figure 8 we saw strengthening and deepening of the AMOC cell under MP boundary conditions. We expect that the intensified AMOC is related to positive density anomalies caused by increased salinity in areas of DWF in the NA. This increase in salinity would be a response to the MP boundary conditions. We indeed observe in Figure 9(a) and 9(b) that the closure of the CAA causes a dramatic increase in the SSS of the Irminger Sea as well as in part of the subpolar gyre and Labrador Sea, which are both important regions where NA DWF takes place. The effect of CO_2 doubling on the NA SSS is minimal compared to that of the MP boundary conditions, as can be seen in Figure 9(c) and 9(d).

Besides the increased SSS in parts of the high NA, we also observe that the Arctic Ocean surface freshens significantly as a result of MP boundary conditions (Figure 9(a) and (b)). We expect that this can be attributed to a combination of factors: a strongly reduced sea ice cover in the MP (Supplementary Figure 2 and 1) and an increase in precipitation over the Arctic. The reduction in sea ice and increase in precipitation are a result of the drastically reduced GIS in the MP. The virtual absence of the GIS causes a sharp decrease in albedo over Greenland, raising the SAT over the Arctic (Supplementary Figure 3). This raise in temperature inhibits sea ice formation over the Arctic Ocean, which in turn drives surface temperatures up further through positive albedo feedback. The warmer air temperatures bring about an increase in precipitation over the Arctic region.

The effect of MP boundary conditions on the freshwater fluxes and transport in the Arctic and NA is further explored in Figure 10. Here, we compare the balance of freshwater into and out of the Arctic for the PI E^{280} and MP Eoi^{280} runs, excluding any possible effects from CO_2 increase. Using Figure 10(a) and 10(b) we are able to compare the spatial differences in average surface freshwater flux, which consists of the evaporation subtracted from the precipitation and runoff (P+R-E). There we observe that the MP boundary conditions, in particular the absence of the

GIS, induce a significant increase in freshwater flux over the entire Arctic. This is likely due to the combination of increased runoff from precipitation over Greenland into the Arctic Ocean and a general increase in precipitation over the Arctic. In addition to the increase in Arctic surface freshwater flux, the absence of the GIS causes a strong reduction in ice sheet runoff from southeast Greenland. The large increase in Arctic precipitation is quantified in Figure 10(c), which shows that the average yearly total Arctic Ocean surface freshwater flux doubles from 0.16 Sv in E^{280} to 0.32 Sv in Eoi^{280}.

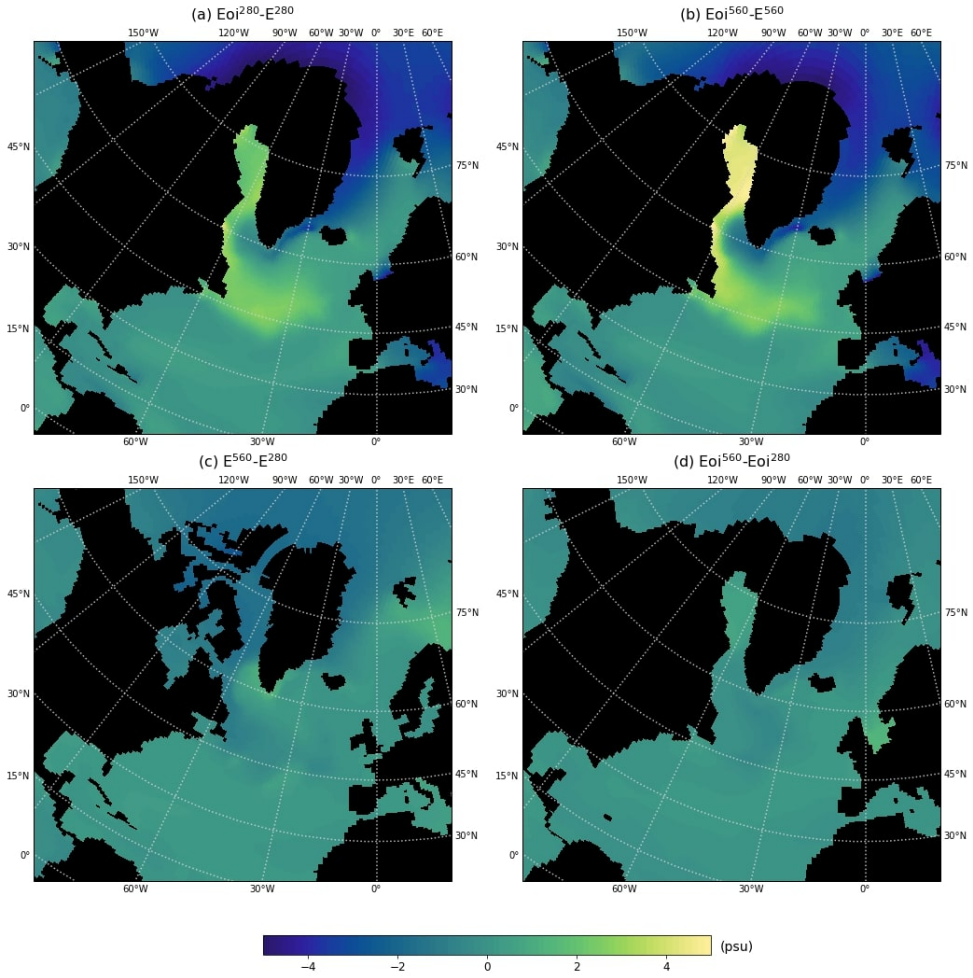

Figure 9: Average simulated North Atlantic sea surface salinity differences between (a) Eoi^{280}-E^{280}, (b) Eoi^{560}-E^{560}, (c) E^{560}-E^{280} and (d) Eoi^{560}-Eoi^{280}.

The large increase in SSS in the Irminger and Labrador Sea can be explained by the closure of the CAA, blocking the export of freshwater from the Arctic into the NA through this passage. Figure 10(c) illustrates that approximately half of the total freshwater transport from the Arctic Ocean into the NA is through the CAA in the PI E^{280} simulation. As there is no freshwater transport through the CAA in the Eoi^{280} simulation, all freshwater into the NA is transported through the indicated G-E section. We also find that the increase in total surface freshwater flux into the Arctic Ocean in Eoi^{280} is larger than the freshwater transport through the BS in E^{280}. Therefore, the average yearly freshwater transport into the NA as a whole increases in response

to MP boundary conditions: 0.25 ± 0.01 Sv in E^{280} and 0.31 ± 0.04 Sv in the Eoi^{280}. Of the freshwater transport through the G-E section, 58% is through the Denmark Strait in Eoi^{280}, as opposed to 40% in the E^{280}. This shows that the distribution of freshwater transport through the Arctic section also changes in response to these boundary conditions.

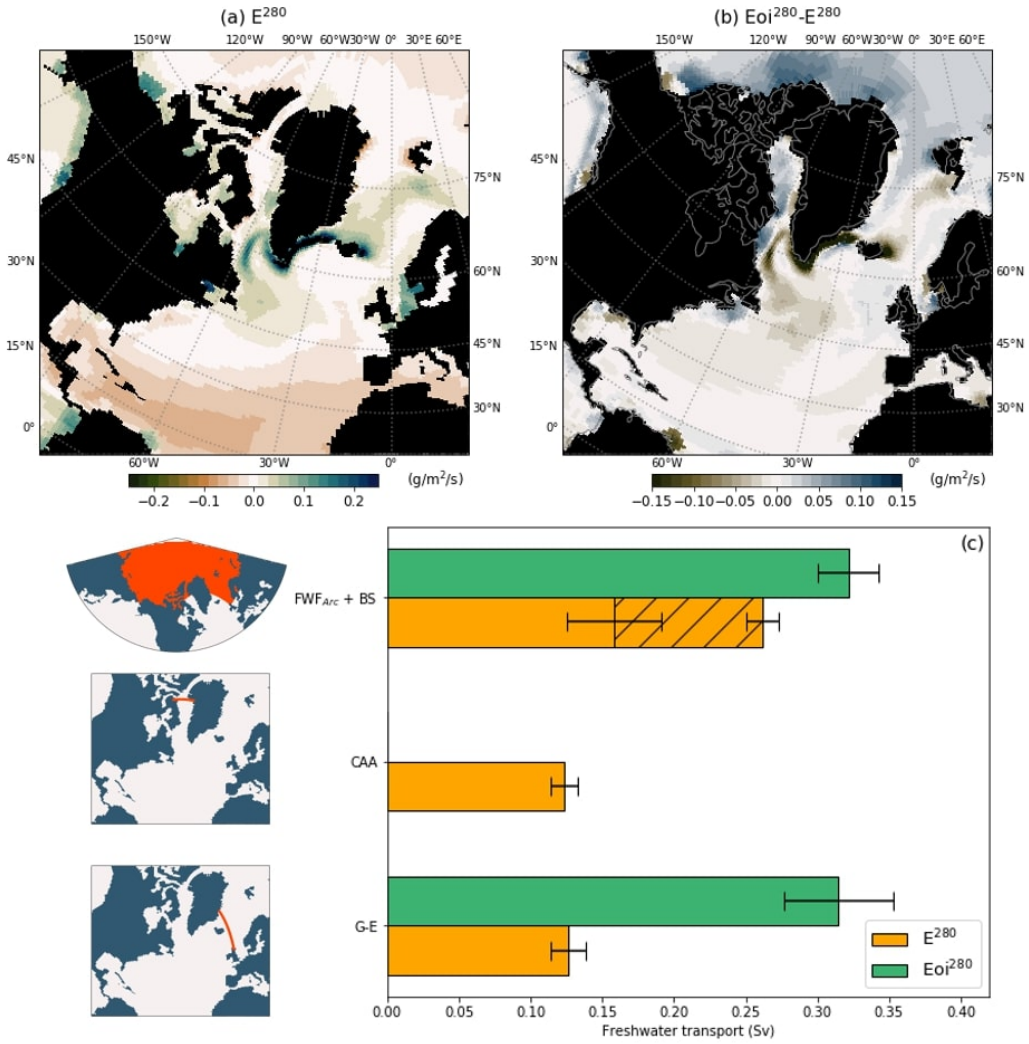

Figure 10: Average yearly NA ocean surface freshwater flux in (a) E^{280} and (b) Eoi^{280}-E^{280}. (c): Yearly total surface freshwater flux into the Arctic (FWF_{Arc}) added to the yearly freshwater transport into the Arctic through the BS, which is indicated by the hatched portion. Yearly freshwater transport out from the Arctic to the NA through indicated CAA and G-E transects. Error bars show the standard deviation.

Earlier we found that the closure of the CAA in the MP simulations strongly increases the salinity of the Labrador Sea. The Labrador Sea is a crucial area with respect to DWF driving the AMOC. DWF takes place mostly in winter, when strong cooling at the surface causes convective instability in the upper ocean. The convective instability gives rise to vertical columns in which strong vertical mixing takes place, driving DWF. These areas in which DWF takes place can be visualized with the mixed layer depth (MLD), which is the depth to which a vertical column of

water has an almost uniform density. Figure 11 shows the 200-year average daily maximum MLD in the NA for each CCSM4-Utrecht simulation. The contours mark the areas where the maximum MLD exceeds 250 m, which we consider areas where it is likely that DWF takes place in winter. We can see significant shifting of DWF areas between the PI and MP simulations: DWF around the coast of Greenland ceases and shifts to the south of the Labrador Sea. The shallowing of the MLD around the Greenland coast is likely due to the increased freshwater transport through Denmark Strait. The new DWF areas we now find in the southern Labrador Sea correspond with the spatial distribution of increased salinity we saw in Figure 9. This confirms that the MP boundary conditions induce altered salinity distributions in the NA that shift NA DWF areas, which is possibly related to the stronger and deeper MP AMOC.

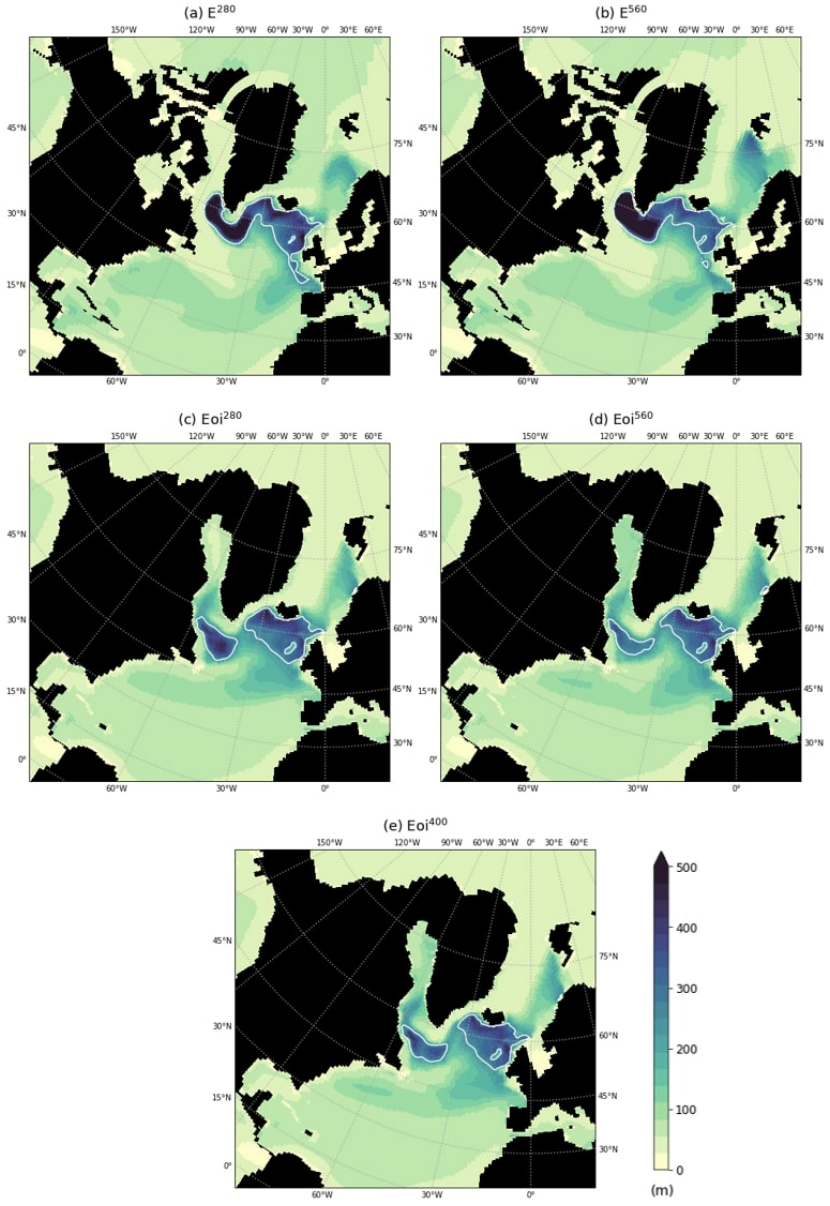

Figure 11: Average simulated NA maximum MLD for (a) E^{280}, (b) E^{560}, (c) Eoi^{280}, (d) Eoi^{560} and (e) Eoi^{400}. White contours indicate MLD $>$ 250m.

3.3 Enhanced warming of mid-Pliocene North Atlantic SSTs

In the MP Eoi^{400}, the average global SST increases by 3.4°C compared to the PI E^{280} simulation. When only considering the NA, average warming increases to 5.1 °C. This enhanced warming in the NA originates mainly from warming in the Labrador Sea and subpolar gyre (Figure 12(b)), with local maxima up to 12.1°C. Other locations with enhanced SST warming can be seen around areas of sea ice in E^{280} that has retreated in Eoi^{400} (Supplementary Figures 1 and 2), as well as some enhancement in the Northern Pacific Ocean. However, it is clear that the greatest warming amplification occurs in the high NA. This is an area where so-called warming holes have previously been identified in simulations as a response to a weakening AMOC (Drijfhout et al., 2012), indicating that the strengthened AMOC in the MP simulations is a likely cause for the amplification of warming we observe in the high NA.

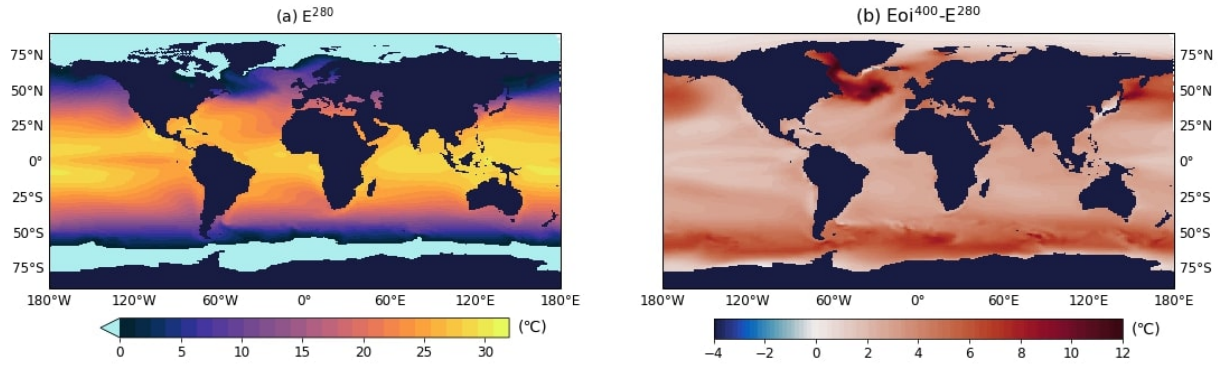

Figure 12: (a): Average global SSTs in E^{280}. (b): Difference in average global SSTs between Eoi^{400} and E^{280}.

The effects of MP boundary conditions on the NA SSTs are separated from effects of CO_2 doubling in Figure 13. This confirms that the enhanced high NA SST warming occurs only as a response to the MP boundary conditions and not as a response to CO_2 increase. In fact, we observe a slight warming hole in Figure 13(d) when doubling CO_2 in the MP simulations, which may be related to the weaker AMOC in Eoi^{560} compared to Eoi^{280}.

We expect to find a higher northward ocean heat transport by the stronger MP AMOC in order to explain the amplification of SST increase in the high NA. In Figure 14, the strength of the mean component of the yearly AOHT associated with the overturning circulation $\overline{\text{AOHT}}_{ov}$ is plotted against the AMOC strength. We see that there is indeed a higher average $\overline{\text{AOHT}}_{ov}$ strength in the MP simulations than the PI simulations. The average $\overline{\text{AOHT}}_{ov}$ at 40°N in E^{280} is 0.66 PW and the differences in $\overline{\text{AOHT}}_{ov}$ strength between the MP simulations and E^{280} are +0.18 PW for Eoi^{280}, +0.20 PW for Eoi^{400} and +0.16 PW for Eoi^{560}. There is no significant difference between the $\overline{\text{AOHT}}_{ov}$ strength in E^{560} and E^{280}.

When we perform a linear regression on the $\overline{\text{AOHT}}_{ov}$ strength and the AMOC strength in the MP and PI simulations, we find that for E^{280}, Eoi^{400} and Eoi^{560} the slopes are virtually identical. These are also the simulations that have run the longest and are thereby most likely to be near equilibrium. Therefore, we may conclude that the increase in AMOC strength in the MP is accompanied by a linear increase in associated ocean heat transport. The linear relationship

follows the classical scaling from equation 2.4 if we assume that the ΔT between northward and southward flowing water is constant in the PI and MP. This assumption may explain why the slopes in the shorter runs deviate: they have had less time to evenly distribute heat over the ocean. Overall, these results suggest that the intensified MP AMOC enhances heat transport to the high NA where the SST increases substantially as a response.

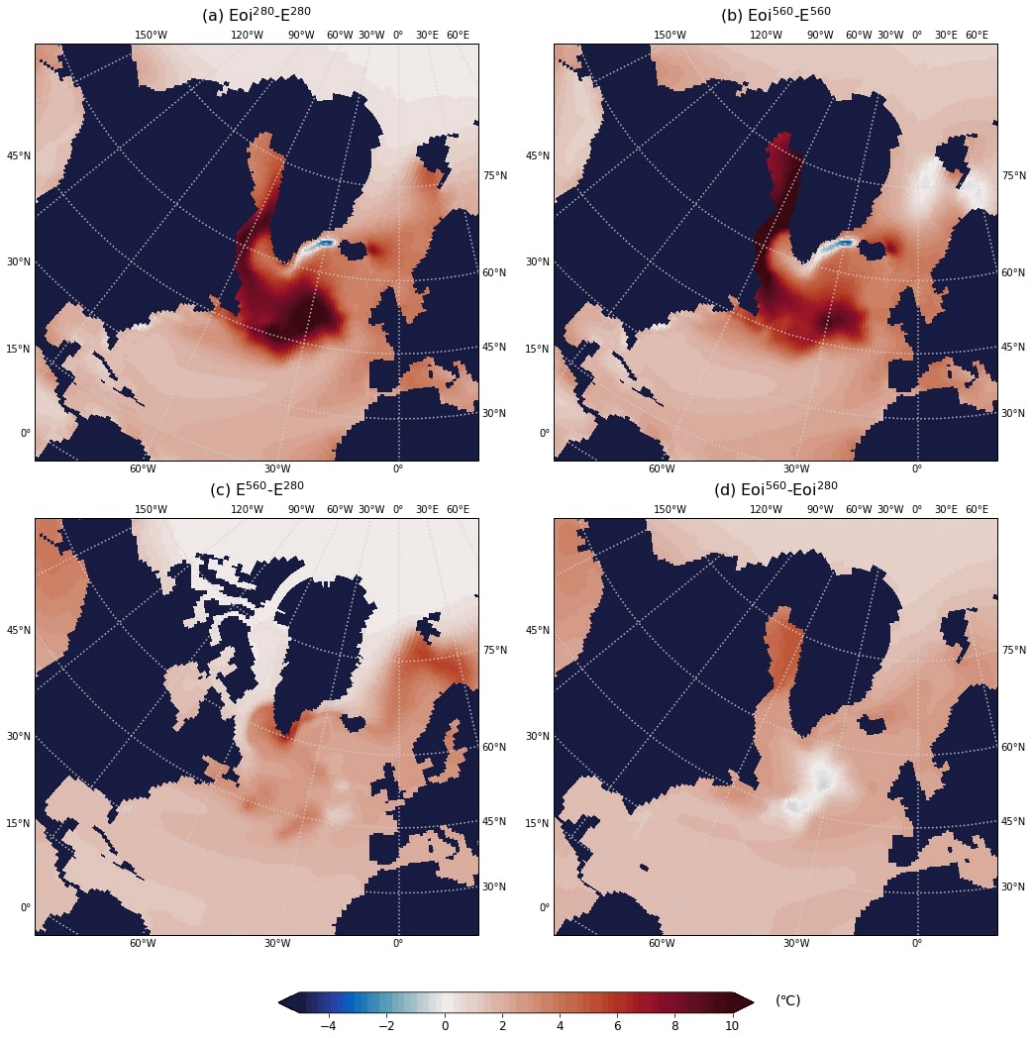

Figure 13: Average simulated North Atlantic SST differences between (a) Eoi^{280}-E^{280}, (b) Eoi^{560}-E^{560}, (c) E^{560}-E^{280} and (d) Eoi^{560}-Eoi^{280}.

To give further insight into the different meridional heat transport processes taking place in the MP Eoi^{400} and PI E^{280} simulations, Figures 15 (a), 15(b) and 15(c) show their 200-year average meridional heat transport components at each latitude. In Figure15(a) we observe that the THT derived by the TOM radiative balance decreases in the Eoi^{400} with respect to E^{280}, especially in the midlatitudes. This decrease in THT is dominated by a decrease in AHT of a similar magnitude, which is caused by the reduced atmospheric meridional temperature gradient in Eoi^{400}. On the other hand, the global OHT appears to be virtually constant.

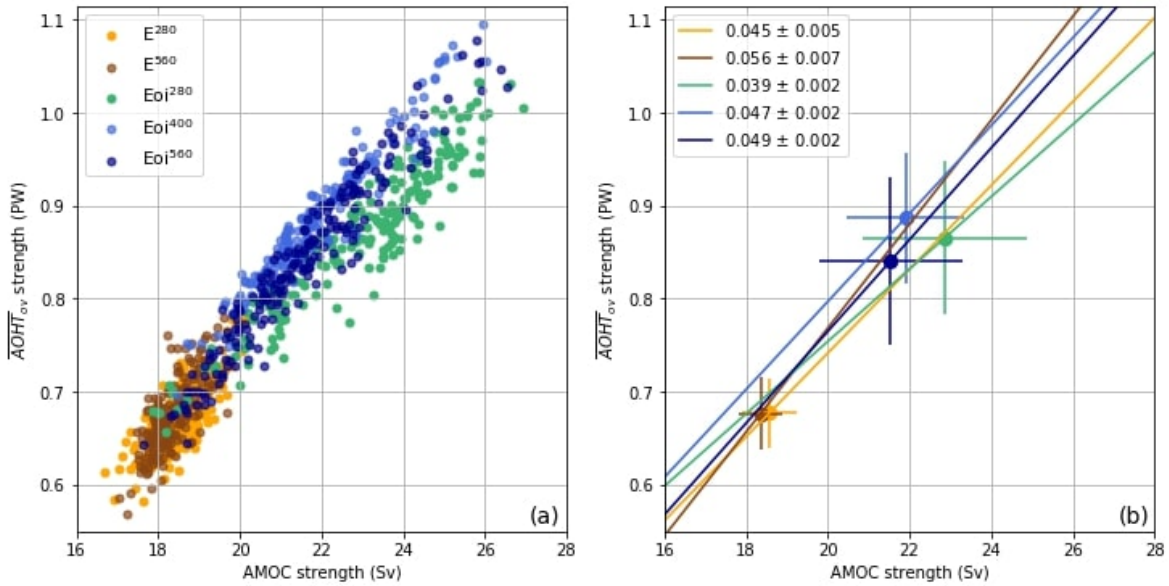

Figure 14: (a): Yearly $\overline{\text{AOHT}}_{ov}$ at 40°N plotted against the AMOC strength at 40°N. (b): Linear regression on yearly data from subfigure (a). The regression slopes and their 95% confidence interval are given in the legend. Markers and error bars respectively indicate the mean and standard deviation.

Figure 15(b) confirms the relatively small changes in global OHT, especially in the NH. However, here we can also see that there is an AOHT increase in Eoi^{400} that is often compensated by a decrease in the Indo-Pacific OHT (IPOHT). When we then split the AOHT into its mean overturning $\overline{\text{AOHT}}_{ov}$, mean azonal $\overline{\text{AOHT}}_{ov}$ and transient eddy component AOHT' in Figure 15(c), it appears that the azonal and overturning components also partially compensate each other and thereby keep the total AOHT relatively constant. The increase in $\overline{\text{AOHT}}_{ov}$ and $\overline{\text{AOHT}}_{az}$ magnitude between 0-40°N implies strengthening of both the heat transport associated with the AMOC, as we found earlier, as well as strengthening of the subtropical gyre circulation in the MP. We also note that both the overturning and azonal components increase in magnitude when their heat transport is in opposite directions. When their heat transport is in the same direction, the azonal component decreases in magnitude, suggesting that the azonal component reacts to changes in heat transport by the overturning circulation in order to keep the total AOHT constant. As expected, we find that the average eddy component is virtually constant between E^{280} and Eoi^{400} as it is associated mainly with seasonal fluctuations (Viebahn et al., 2016).

Even though the PI and MP simulations exhibit a similar relationship between the $\overline{\text{AOHT}}_{ov}$ and AMOC strength, where the stronger AMOC MP causes a concurrent linear increase in $\overline{\text{AOHT}}_{ov}$ strength, there are significant differences in the temporal AMOC and $\overline{\text{AOHT}}$ variability within the simulations. This is highlighted in Figure 15(d) and 15(e), which show the variability of the last 100 years of the strength of the $\overline{\text{AOHT}}$ components and the AMOC strength at 40°N. Here we also observe the compensation between the $\overline{\text{AOHT}}_{ov}$ and $\overline{\text{AOHT}}_{az}$ components that we saw in Figure 15(c), which is especially clear in the MP Eoi^{400} simulation. The most prominent difference between the two figures is that the amplitude and period of fluctuations in AMOC strength and strength of the $\overline{\text{AOHT}}$ components is significantly larger in the MP Eoi^{400} simulation. As we

concluded that the NA SST warming in the MP is likely related to the intensified AMOC, we would expect to find similar changes in temporal behavior in the NA SSTs. In the next section, we will further discuss the variability of the SST associated with the AMOC in the PI and MP simulations.

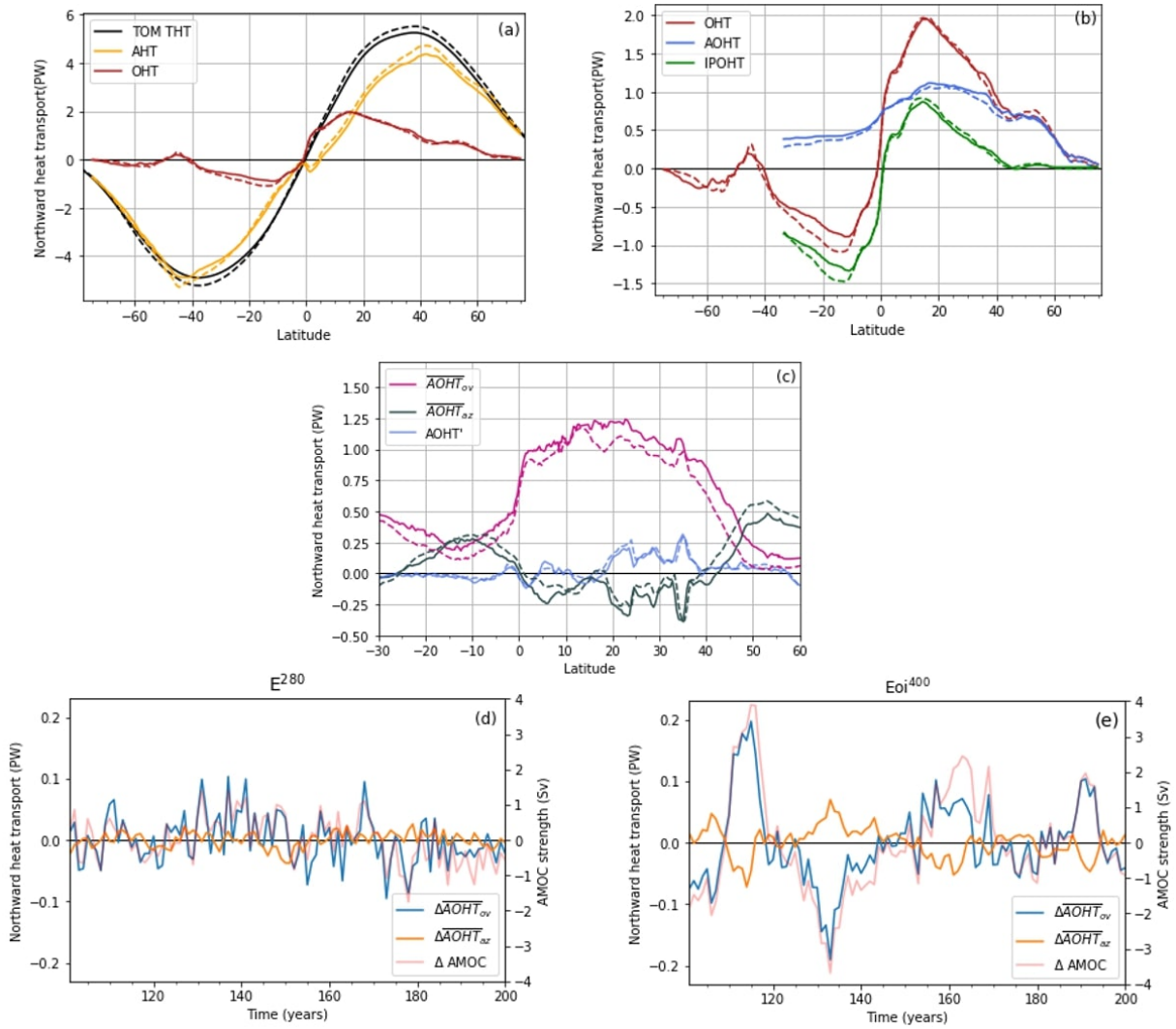

Figure 15: (a): Average total heat transport (THT) at the TOM and the atmospheric (AHT) and ocean heat transport (OHT) components. (b): Average OHT and its Atlantic (AOHT) and Indo-Pacific (IPOHT) components. (c): Average AOHT divided into the mean overturning ($\overline{\text{AOHT}}_{ov}$), mean azonal ($\overline{\text{AOHT}}_{az}$) and transient eddy component (AOHT′). (d): E^{280} time series of AOHT and AMOC anomalies at 40°N. (e): Eoi^{400} time series of AOHT and AMOC anomalies at 40°N. In (a) - (c) solid lines indicate Eoi^{400} and dashed lines indicate E^{280}.

3.4 North Atlantic SST and AMOC variability

The linear relationship between the $\overline{\text{AOHT}}_{ov}$ and AMOC strength in the PI and MP simulations suggests that the intensified AMOC and concurrent increase in associated AOHT is the likely cause of the amplified high NA SST warming we observe. By now extending the analysis to the variability of the SST in the CCSM4-Utrecht simulations, we are able to further examine the relationship between the SST enhancement and AMOC increase in the MP simulations.

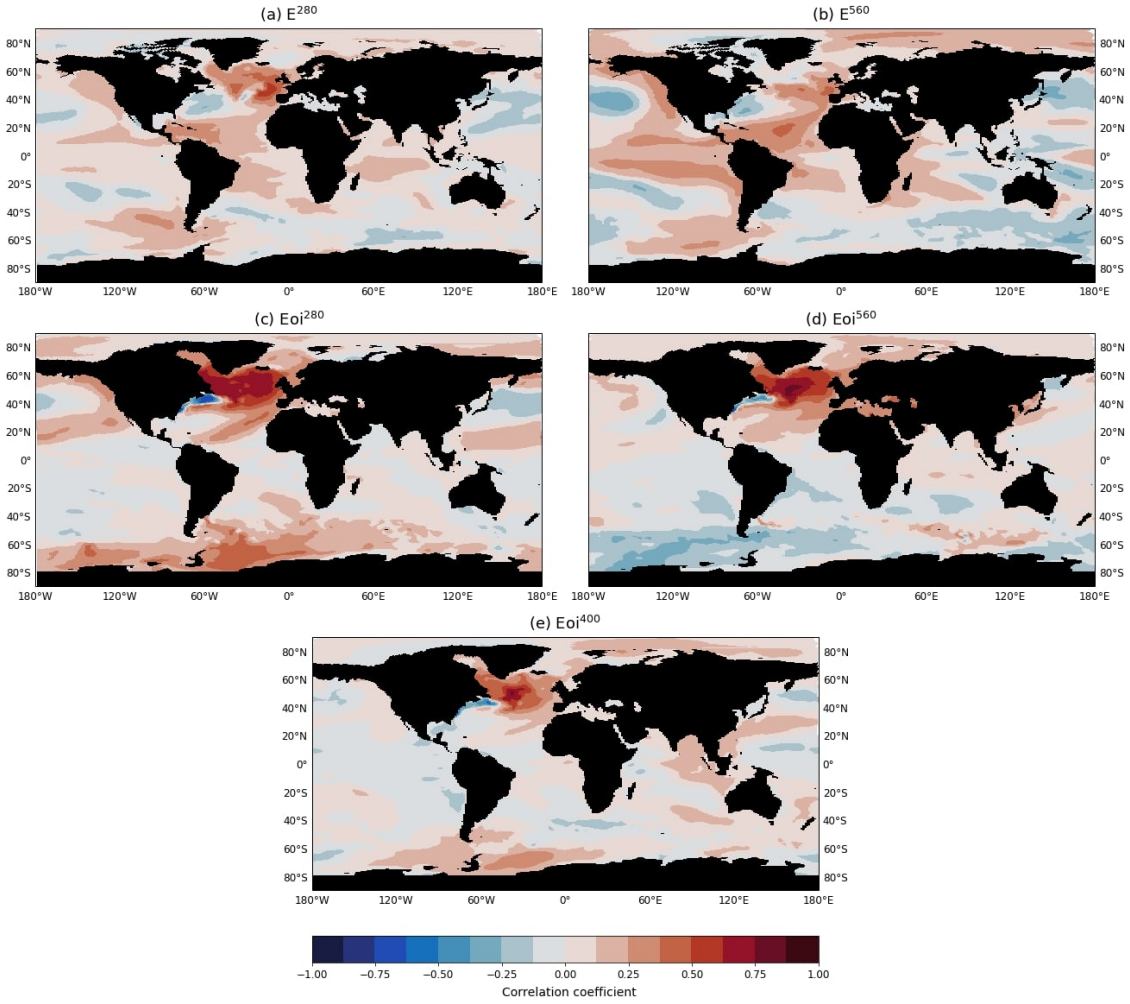

Figure 16: Correlation between the SST and AMOC strength at each grid point for (a) E^{280}, (b) E^{560}, (c) Eoi^{280}, (d) Eoi^{506} and (e) Eoi^{400}. Supplementary Figure 4 indicates the areas where the correlation is above the 95% confidence level.

Figure 16 shows the correlation of the SST at each grid point with the AMOC strength at 40°N for all simulations. The PI and MP simulations show a distinctly different pattern in the NA, yet this pattern is consistent within the PI and MP group of simulations. In all MP simulations we observe a strong correlation between subpolar gyre SSTs and the AMOC as well as a high anti-correlation between SSTs in a narrow band off of the Gulf Stream region and the AMOC. This typical SST fingerprint of the AMOC (Caesar et al., 2018) supports our earlier conclusion that it is the stronger MP AMOC driving the enhanced NA SST warming. The high correlation

with subpolar gyre SSTs is absent in the PI simulations and a substantial part of the correlation that we find in the PI NA is not significant above the 95% confidence level (Supplementary Figure 4). This suggests that the behavior of the AMOC as a response to MP boundary conditions is fundamentally different from the behavior of the PI AMOC.

Further analysis of the NA SST variability is shown in Figure 17. Figures 17(a) - (c) show the three leading empirical orthogonal functions (EOFs) of the NA SSTs in E^{280} and Eoi^{400}. The three EOFs combined are responsible for respectively 48% and 41% of all NA SST variability in E^{280} and Eoi^{400}. Figures 17(d) - (f) also show the Multi-Taper Method (MTM) (Thomson, 1995; Percival et al., 1993) power spectra associated with the three leading standardized principal components (PCs) of the E^{280} and Eoi^{400} NA SST field. These spectra give insight into the times scales associated with the NA SST variability that is observed in the three leading EOFs. Along with the spectra, the correlation coefficient between the AMOC strength and PC and the correlation coefficient between the AMO index and PC is shown.

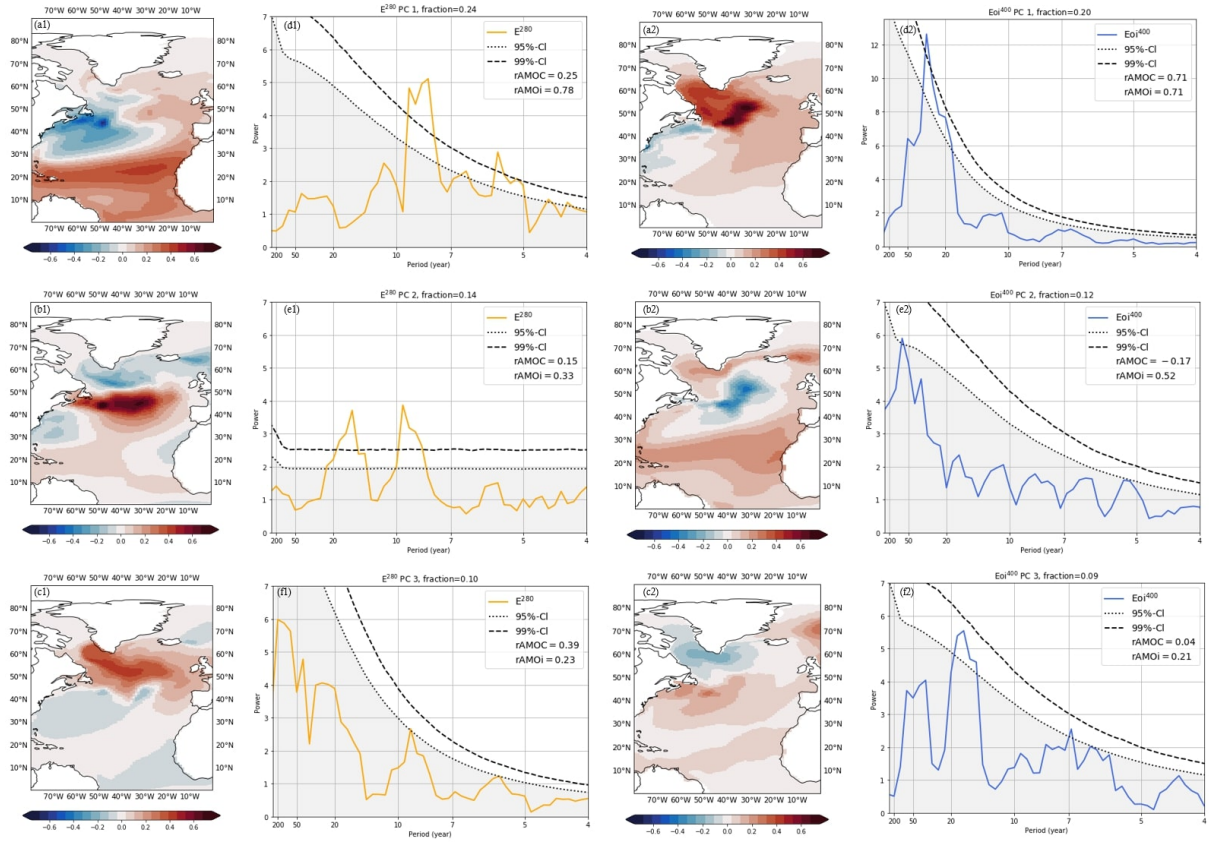

Figure 17: (a1) - (c1): Three leading EOFs of E^{280} with in (d1) - (f1) the MTM power spectra of their corresponding standardized PCs. (a2) - (c2): Three leading EOFs of Eoi^{400} with in (d2) - (f2) the MTM power spectra of their corresponding standardized PCs. The correlation between the PCs and the AMOC strength and AMO index is shown in the legend of each individual PC MTM spectrum. The dotted line and shading indicates the 95% confidence level and the dashed line indicates the 99% confidence level, both using red noise as the null hypothesis. Refer to Supplementary Figures 5 and 6 for PC Fourier spectra.

The PCs of the leading modes of E^{280} and Eoi^{400}, which contain respectively 24% and 20% of the NA SST variability, show a peak period of approximately 8 years for E^{280} and 28 years for Eoi^{400}. The power of the Eoi^{400} peak is more than double the power than that of the E^{280} peak. These features resemble the same behavior as that of the $\overline{AOHT}$ and AMOC strength variability in Figures 15(d) and (e): larger amplitude and periods of variability in Eoi^{400}. While the leading PC in E^{280} does not significantly correlate with the AMOC strength, this correlation is very strong with the leading Eoi^{400} PC. In addition, the leading EOF of the Eoi^{400} NA SST field shows a close resemblance to the correlation pattern of the SST and AMOC strength in Figure 16(e) and the positive anomaly is in the same location as where we find the amplified NA warming in the MP. This leads us to conclude that there is a strong dominant mode of NA SST variability in Eoi^{400} associated directly with the AMOC. The same type of variability is possibly also present in the third E280 mode, albeit much less dominant and less strongly correlated with the AMOC strength than in Eoi^{400}. It does show significant variability at approximately the same timescale as the leading E^{280} mode, suggesting a connection between the variability associated with the AMO and AMOC in the respective first and third mode.

In the leading EOF of E^{280}, we find a pattern that corresponds well to the AMO pattern identified by Kushnir (1994). Supported by a strong correlation of its associated PC with the AMO index, it is likely that the leading mode of NA SST variability in the PI E^{280} is the AMO even though we do not find the classic 20-30 and 50-70 year timescales of multidecadal variability in its PC spectrum. In the MP, we find that the leading PC component in Eoi^{400} also correlates well with the AMO index but contrary to the PI leading PC it correlates equally well with the AMOC strength. This suggests that in Eoi^{400} the SST variability associated directly with the AMOC exerts a much more dominant influence on NA SSTs in Eoi^{400} than in E^{280}. While the leading Eoi^{400} EOF does not show the classic AMO pattern, the second EOF does show a moderately similar AMO pattern to that of E^{280} and the second PC also correlates quite well with the AMO index. In addition, we see a marginally significant peak arising at 66 years, which is a typical AMO timescale. Thus, it is likely that the AMO variability is still present in the Eoi^{400} but less dominant and atypical in its spatial pattern. Instead, the NA mean SST in Eoi^{400} is dominated by the AMOC rather than the AMO.

The remaining respective second and third mode of variability in E^{280} and Eoi^{400} show a similar EOF pattern and both have significant peaks in their PC power spectra. However, as we are not able to attribute their variability to the AMOC or AMO due to low correlations, we will disregard these modes of variability in this analysis.

Given these results, we consider the first and third modes of respectively Eoi^{400} and E^{280} leading modes in variability of NA SSTs directly related to behavior of the AMOC. The longer peak period in the Eoi^{400} simulation confirms the lower frequency variability of the SSTs and AMOC in the MP compared to the PI. In addition, the relatively strong correlation between the AMOC strength and the leading PC in Eoi^{400} reinforces our conclusion that it is the AMOC driving the enhanced warming in the high NA. Both the difference in their leading EOFs and the longer peak period in SST variability associated with the AMOC again suggest that the MP AMOC behaves in a fundamentally different way than the PI AMOC. In the final subsection, we will attempt to explain this change in behavior.

3.5 Mid-Pliocene freshwater flux sensitivity

The larger amplitude and longer peak periods we observe in the Eoi^{400} AMOC variability may be the result of a weaker negative feedback between the ocean temperature in the high NA and the AMOC strength in the MP. Normally, a strengthened AMOC causes more heat and salt to be transported northwards. The salt feedback is positive as a higher salinity in the high NA causes a stronger AMOC. On the other hand, the temperature feedback is negative: increased temperatures in the high NA result in reduced convection and a weakened AMOC. In the MP simulations we see that even though there is a much higher temperature in the high NA than in the PI, we still observe a stronger AMOC due to increased salinity. Based on this finding, we expect that the MP AMOC is more strongly driven by salinity and the negative temperature feedback is weakened. Therefore, when anomalies in NA salinity result in a response in the AMOC, this response is amplified due to the dominance of the salinity feedback. As a result, larger anomalies in AMOC strength and NA SST are able to build up for a longer time in the MP compared to the PI.

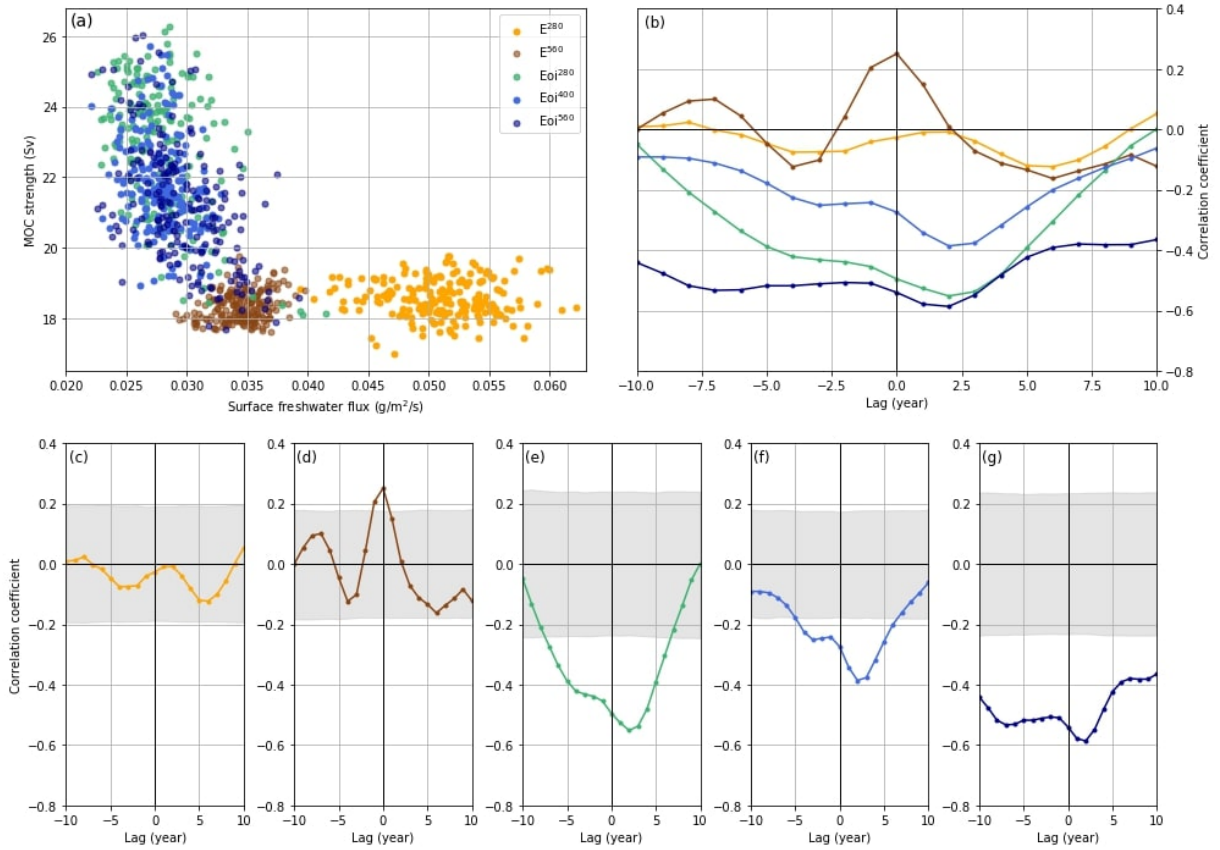

Figure 18: (a): 3-year running mean AMOC strength plotted against the 3-year running mean average surface freshwater flux in the Labrador Sea. (b): Correlation coefficients for each simulation between the 3-year running mean AMOC strength and 3-year running mean Labrador Sea freshwater flux. A positive lag indicates that the surface freshwater flux leads the AMOC. (c) - (g): Individual correlation coefficients for E^{280}, E^{560}, Eoi^{280}, Eoi^{400} and E^{560}, respectively. Shading indicates the 95% confidence interval using red noise as the null hypothesis. Refer to Supplementary Figure 7 for results of the unfiltered time series.

If the MP AMOC is driven mainly by the high Labrador Sea salinity in the MP, we expect that the AMOC will be more sensitive to the surface freshwater flux in the Labrador Sea. This is confirmed in Figure 18(a), where the time series of the yearly average surface freshwater flux in the Labrador Sea is plotted against the AMOC strength. A 3-year running mean filter is applied to both time series as the surface freshwater flux is relatively noisy and we only expect an effect from significant anomalies in surface freshwater flux. In Figure 18(a) we do not see any relationship between variability in the surface freshwater flux and the AMOC strength in the PI simulations. On the other hand, in all MP simulations we observe that a reduction in surface freshwater flux appears to be related to a stronger AMOC. In Figure 18(b) - (g) we find the expected anti-correlation between the AMOC strength and the surface freshwater flux in the Labrador Sea for all MP simulations above the 95% confidence level at lag 0. This anti-correlation increases in magnitude and significance as the AMOC lags 1-2 years behind the surface freshwater flux, suggesting that the AMOC responds with a delay to the anomalies in salinity caused by the surface freshwater flux. In the PI simulations, we do not see correlations that are above the 95% confidence levels except for correlation in E^{560} that is marginally above the confidence interval. These results support our hypothesis that the simulated MP AMOC is more strongly driven by salinity than the PI AMOC.

4 Discussion

In our study we found that the MP AMOC intensifies due to the closure of the CAA, inhibiting freshwater transport into the Irminger and Labrador Sea. This causes a sharp increase in salinity in the southern Labrador Sea, shifting part of the NA DWF areas to this location. These results generally agree with the conclusion of Otto-Bliesner et al. (2017) that the closure of the BS and CAA results in a stronger AMOC. A more recent study on the COSMOS model of the PlioMIP2 ensemble also found that the AMOC in the COSMOS Eoi^{400} simulation weakens when the NH gateways are opened (Stepanek et al., 2020). Nevertheless, our findings do differ from Otto-Bliesner et al. (2017) in terms of the mechanism responsible for the strengthening AMOC. They identified that the closure of the BS is essential for strengthening the AMOC as this causes the Arctic to become saltier, decreasing the total freshwater transport into the NA. However, in our results we found that increased precipitation due to the absence of the GIS increases the total volume of freshwater transport from the Arctic into the NA. This means that our results do not agree with the conclusions of Otto-Bliesner et al. (2017), who found that exclusively closing the CAA and not the BS weakened the AMOC. Therefore, we must be careful to attribute our findings solely to the closure of the Arctic gateways and consider that there are other MP boundary conditions, in particular the absence of the GIS, that also play a role. We saw that the GIS strongly impacts the NA and Arctic precipitation, runoff and surface air temperature. Further sensitivity studies would be useful in order to separate the effects of the different MP boundary conditions. The inability to do this with the available simulations is a limitation of this study.

The amplified high NA SST in warming in CCSM4-Utrecht is found to be as a response to MP boundary conditions. Furthermore, we observe that the AOHT associated with overturning increases linearly as a response to the AMOC strength, following the classical scaling relationship. The simulations that have a shorter spin-up time, E^{560} and Eoi^{280}, have a slope that deviates slightly, possibly due to a more uneven vertical distribution of ocean heat. Further investigation into the relationship between the AMOC and $\overline{\mathrm{AOHT}}_{ov}$ may be useful, as the assumption that the temperature gradient between the northward and southward flowing water stays the same in the PI and MP is quite crude. In fact, results comparing the different mixing schemes in the PI and MP simulations show that this temperature gradient may be affected (Appendix A). It should also be noted that the relationship between the AMOC strength and $\overline{\mathrm{AOHT}}_{ov}$ changes when it is examined at a latitude where there is substantially more eddy activity by wind-driven circulation, such as at 35°N. We expect that this is a result of the separation of $\overline{\mathrm{AOHT}}$ into overturning and wind-driven components, which is not free of error. In addition, there is a significant eddy component AOHT$'$ at these latitudes that may also induce some error. Our analysis at 40°N, where there is little eddy activity, provides a solid basis for our conclusion that it is the AMOC driving enhanced high NA SST warming. However, further investigation into the behavior of the different AOHT components could provide valuable information about possible differences between the PI and MP simulations in the dynamics of the ocean heat transport and ocean-atmosphere interactions.

Our findings contradict the conclusion of Zhang et al. (2021) that the mid-Pliocene warmth simulated in the PlioMIP2 ensemble is not driven by an intensified AMOC and concurrent enhanced OHT. This may be caused by the methods with which the models are analyzed, as Zhang et al. (2021) did not separately examine the AOHT associated with overturning. We saw in our analysis that the increase in the MP $\overline{\mathrm{AOHT}}_{ov}$ was partly compensated by $\overline{\mathrm{AOHT}}_{az}$, thereby

keeping the total AOHT relatively constant. Separating these components in the PlioMIP2 ensemble could provide more insight into whether this behavior also occurs in other members of the ensemble and possibly affects the results. It should be noted that CCSM4-Utrecht was one of the models with the highest NA SST anomalies of the PlioMIP2 ensemble and its behavior may not be representative for the other participating models. Nevertheless, our analysis does provide strong evidence that the intensification of the AMOC is in fact the driver of the high NA warming in the CCSM4-Utrecht model.

Finally, the analysis was extended to include the temporal variability of the SSTs associated with the AMOC. The results strengthen the conclusion that the amplified warming in the MP is driven by a stronger AMOC. We note that the dominant time scale of the AMO-patterened variability that we see in the E^{280} NA SSTs is shorter than the 20-30 year and 50-70 year time scales that are typically associated with the AMO (Frankcombe et al., 2010). The fact that we do not see these longer time scales represented may be a result of the resolution of the model: Jüling et al. (2020) found when the CESM1 resolution is increased such that it can resolve mesoscale ocean flows, multidecadal variability in the NA becomes more pronounced and matches observations better. In the MP Eoi^{400} simulation, we find a dominant time scale of 66 years in NA SST variability associated with an AMO pattern, which is within the range of the 50-70 year AMO time scale. However, this is not the leading mode of variability in the MP. The leading EOF in Eoi^{400} does not show the typical AMO pattern and is more likely related to strengthening and weakening of the AMOC itself. Overall, we find that the dominant MP NA SST variability associated with the AMOC has a larger amplitude, longer period and a different spatial pattern than its PI counterpart. We attempt to explain this by our hypothesis that the MP AMOC shifts to a regime that is strongly dominated by salinity anomalies. When we correlate the AMOC variability with the surface freshwater flux, the behavior of the AMOC does appear to be much more sensitive to the surface freshwater flux in the MP. This would be expected if it is driven more strongly by salinity rather than temperature. Therefore, the dominant variability we observe in the MP may be related to the atmospheric noise and freshwater exchange between the Arctic and NA Ocean, of which the timescale identified by Frankcombe et al. (2010) is 50-70 years. It is possible that increasing the model resolution will also highlight this type of multidecadal variability in the leading mode of variability in the MP.

5 Conclusion

To be able to answer the first research question we compared the different MP and PI simulations to examine what is driving the stronger MP AMOC. The results show that the intensified MP AMOC in the CCSM4-Utrecht simulations is driven by MP boundary conditions prescribed by the PRISM4 reconstruction. The closure of the CAA inhibits one of the two freshwater transport pathways from the Arctic to the NA and induces an increase in salinity in the Labrador Sea. In combination with more than doubled freshwater transport though the Denmark Strait, areas where DWF takes place in the Labrador Sea shift southwards in the MP. They relocate from the coast of south Greenland in the PI simulations to the coast of Newfoundland in the MP simulations. The high salinity in these areas of DWF drives the stronger AMOC in the MP.

Next, we investigated whether the stronger AMOC is driving the simulated amplified warming in the high NA in the MP. For this, we considered the relationship between the AMOC strength and the strength of the AOHT associated with overturning. We were able to find a consistent linear relationship between the AMOC and $\overline{\text{AOHT}_{ov}}$ strength in both the PI and MP simulations. In addition, correlation maps between the AMOC strength and SST fields show a pattern of high NA SST warming that strongly correlates with the AMOC strength in the MP simulations. From these results we can conclude that the intensified MP AMOC is in fact the driver of enhanced AOHT, resulting in amplified high NA SST warming in the CCSM4-Utrecht MP simulations.

Finally, we studied the differences in AMOC and SST variability between the PI and MP simulations and attempted to explain these differences. In our results we observed a shift to larger amplitudes and longer time scales in the MP SST variability associated with the AMOC. At the same time, the dominant mode of SST variability shifted from variability associated with the AMO in the PI E^{280} simulation to variability directly related to the AMOC in the MP Eoi400 simulation. Our hypothesis to explain these differences in variability is that the MP boundary conditions, in particular the closure of the Arctic gateways, induce a change in AMOC regime where it becomes more strongly driven by salinity and the temperature feedback weakens. The high sensitivity of the MP AMOC to the atmospheric freshwater flux in the Labrador Sea supports this hypothesis.

A Background vertical diffusivity

In the introduction, the classical scaling relationship between the meridional overturning strength, vertical mixing parameter and meridional density gradient was introduced. We were not able reproduce any consistent relationship between κ_v, which is the total vertical diffusion coeffient in CESM given at every horizontal and vertical ocean gridpoint, and the AMOC strength. The relationship between κ_v and AMOC strength is confirmed in general circulation model studies (Bryan, 1987), however, Jayne (2009) finds that this is only the case when κ_v is homogeneous over the whole water column. In our CESM simulations, κ_v varies greatly over the water column as a result of the KPP scheme. This may explain why we do not find this relationship in any of our simulations.

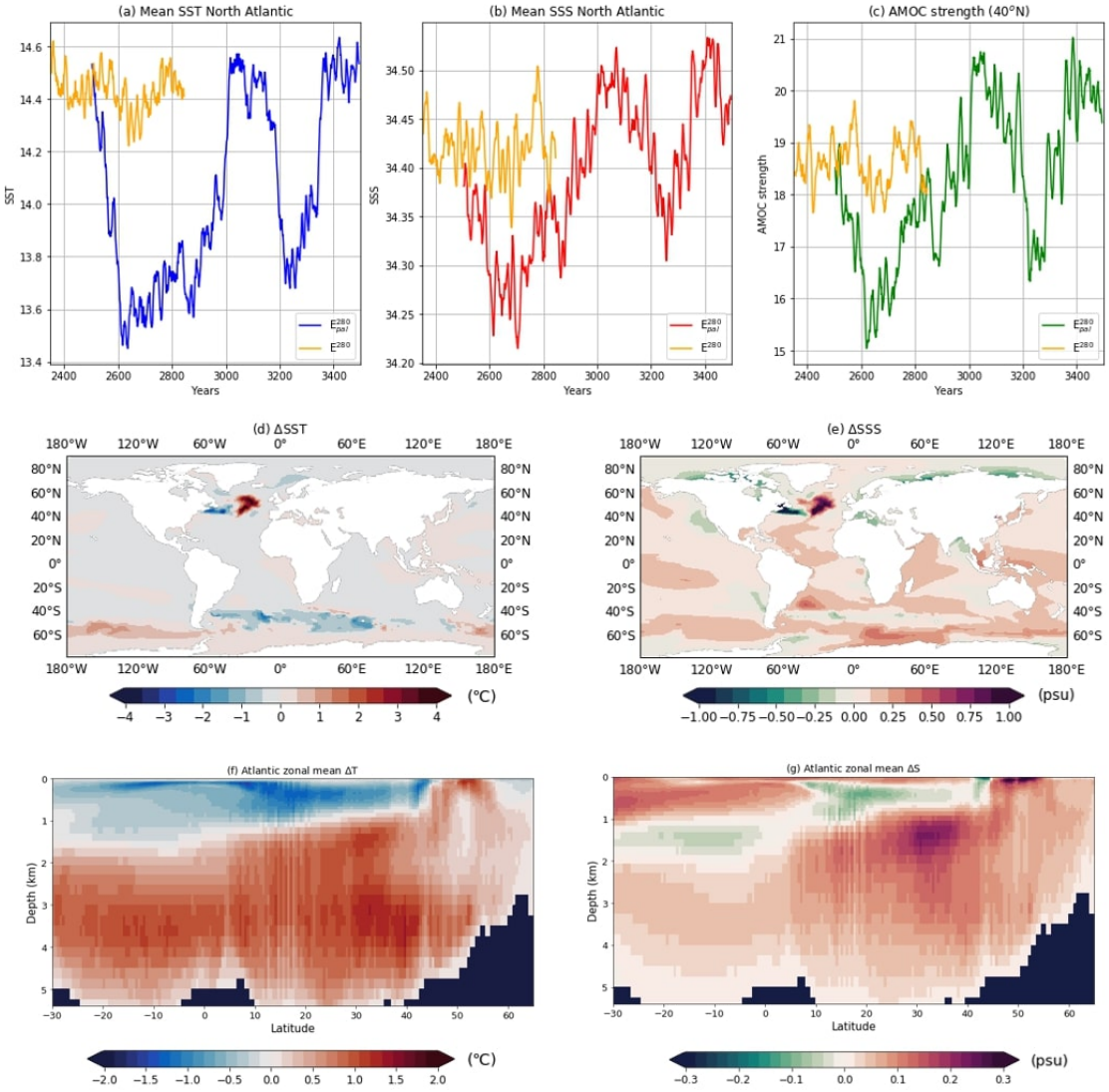

Figure 19: (a) - (c): 10-year running mean of the mean NA SST, mean NA SSS and AMOC strength at 40°N for the last 500 years of the E^{280} and 1000 years of E^{280}_{pal}. (d) - (e): E^{280}-E^{280}_{pal} difference in mean SSTs and SSS of last 200 simulation years. (f) - (g): E^{280}-E^{280}_{pal} difference in zonal mean SSTs and SSS of last 200 simulation years.

The relationship between vertical mixing and the overturning strength is of particular interest due to the difference in the background vertical mixing coefficient in the PI and MP simulations. In chapter 2, we discussed findings of previous studies on the effect of vertical mixing parametrizations on the AMOC and NA and how these pertain to our situation. There, we concluded that the difference in background vertical diffusivity between the PI and MP simulations likely does not have a significant effect on the simulated AMOC or Atlantic ocean heat transport. To verify this, we analyzed an extra E^{280} simulation with the same background vertical mixing parameters as the MP simulations, which we will name E^{280}_{pal}.

Figure 19(a) - (c) shows the temporal evolution of the 10-year running mean of the mean NA SST, SSS and AMOC strength in E^{280}_{pal} compared to that of E^{280}. We see that the fluctuations are much larger in E^{280}_{pal} and that the simulation likely has not reached its equilibrium. While the SST of the last 100 years seems to have settled on a stable level equivalent to that of the E^{280} SST, the SSS and AMOC strength are still drifting. This indicates that when looking at the other results, which are all found using the mean of the last 200 simulation years, we should be cautionary about making any certain conclusions.

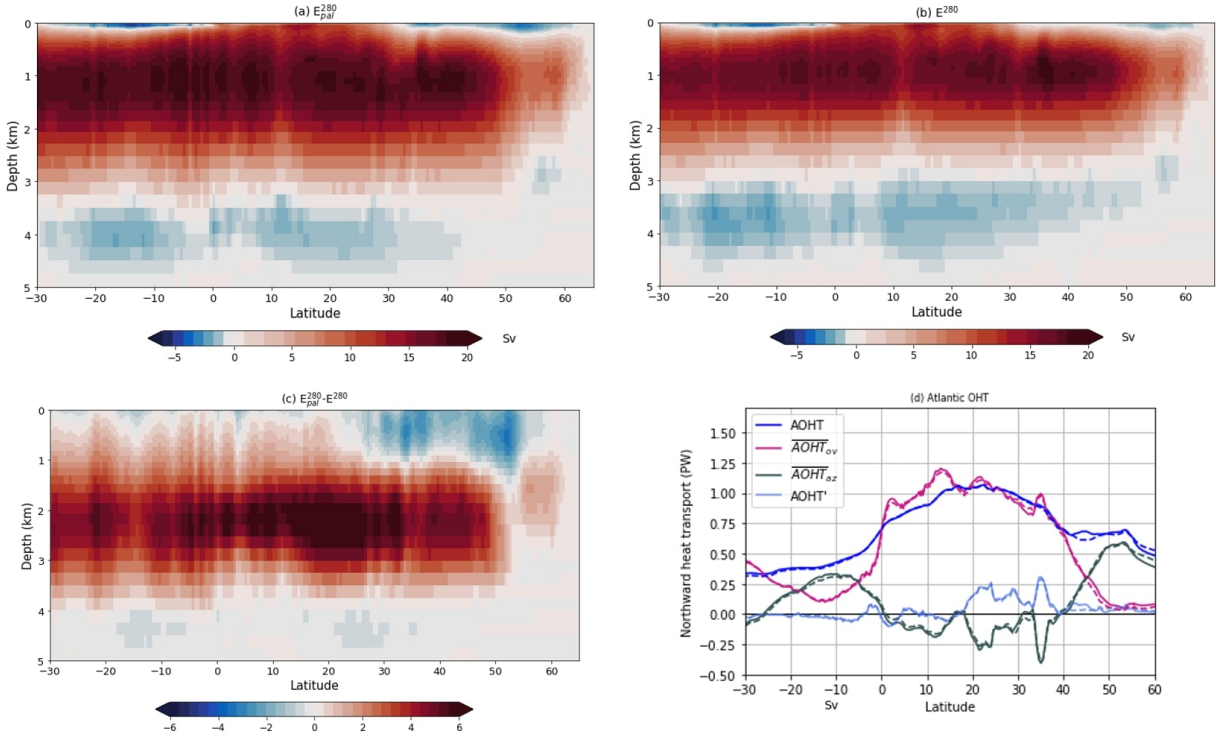

Figure 20: (a) and (b): Mean Atlantic MSF of E^{280}_{pal} and E^{280} respectively. (c): E^{280}_{pal} and E^{280} difference in mean Atlantic MSF. (d): Total Atlantic OHT and its components in both E^{280}_{pal} (solid) and E^{280} (dashed).

In both Figures 19(d) and (e), we see two areas in the NA with significant anomalies in the E^{280}_{pal} SST and SSS. We find that there is cooling and freshening in the Gulf Stream region and warming and saltening in the subpolar gyre region. In addition, Figure 19(f) shows that the majority of the Atlantic Ocean warms up below 1000 m and cools above 1000 m. This is expected since the background mixing coefficient in E^{280}_{pal} is increased at depths below 1000 m, mixing

warmer surface water more efficiently into the deep ocean, and decreased above 1000 m. This may decrease the temperature gradient between northward and southward flowing water of the AMOC in the MP simulations and thereby affect the scaling between the AMOC and $\overline{\text{AOHT}_{ov}}$ strength. We did however not observe such an effect in figure 14. The effect of the altered vertical mixing coefficients on the zonal mean SSS in Figure19 is less clear: the majority of the Atlantic becomes saltier, with the exception of the subsurface in part of the NA and a horizontal band at approximately 1500 m depth in the South Atlantic.

The SST and SSS patterns observed in Figures 19(d) and 19(e) point to a strengthened AMOC in the E_{pal}^{280} simulation, which is what we see in Figure 19(c). The average AMOC strength for the last 200 simulation years is 19.6 Sv in E_{pal}^{280} as opposed to 18.7 Sv in E^{280}. Figures 20(a) - (c) show the 200-year mean Atlantic MSF of E_{pal}^{280} and E^{280} and their difference. There we observe that the E_{pal}^{280} AMOC cell becomes deeper and moderately stronger. It is mostly below 1000 m depth that the MSF intensifies, which is expected as at these depths the background vertical mixing coefficient increases. The effect on the AMOC strength itself appears to be limited: the 0.9 Sv increase in AMOC strength is significant but not nearly as large as the increase we see between the MP and PI simulations, which is an increase of 4.2 Sv in Eoi^{280} from E^{280}. Finally, the mean AOHT and its components were also examined in E_{pal}^{280} and E^{280} (Figure 20(d). Here, we find that there is no significant difference in any of the AOHT components between the E_{pal}^{280} and E^{280} run, even though E_{pal}^{280} has a stronger AMOC.

Overall, we find that using a different mixing scheme in the PI simulations does have an impact on the SST, SSS and AMOC strength, but that the effect on the results from our study is likely limited. Assuming that the E_{pal}^{280} is in equilibrium, there is a strengthening and deepening of the AMOC cell but no effect on the AOHT. We also observe some warming in the high NA, although this is limited in magnitude and spatial extent compared to the warming in the MP simulations. In addition, we find cooling and freshening in the Gulf Stream sea surface as well as saltening in the subpolar gyre. Neither of these features in SSS are observed in any of the MP simulations. Combined with the drift that we find in the data, E_{pal}^{280} is most likely not close enough to equilibrium to make definitive conclusions about the effect of the difference in background mixing coefficients. However, given the data we have, we will for now conclude that the results of the analysis that has been done on the MP simulations are not critically impacted by the difference in background mixing coefficient. The next step will be to run the E_{pal}^{280} for a longer time, compare it again to E^{280} and then repeat the analysis in this study using E_{pal}^{280} instead of E^{280}.

B Supplementary figures

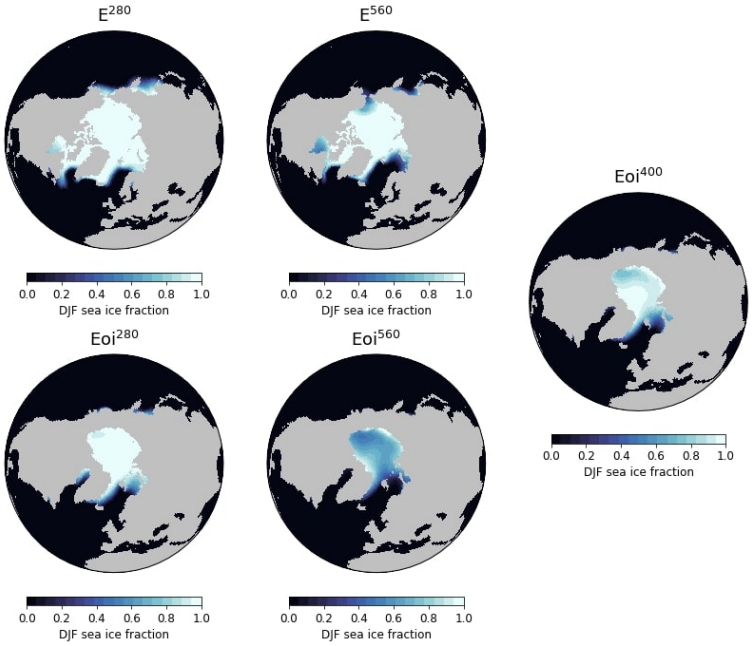

Supplementary Figure 1: Average simulated sea-ice fraction from December to February (DJF) for each simulation.

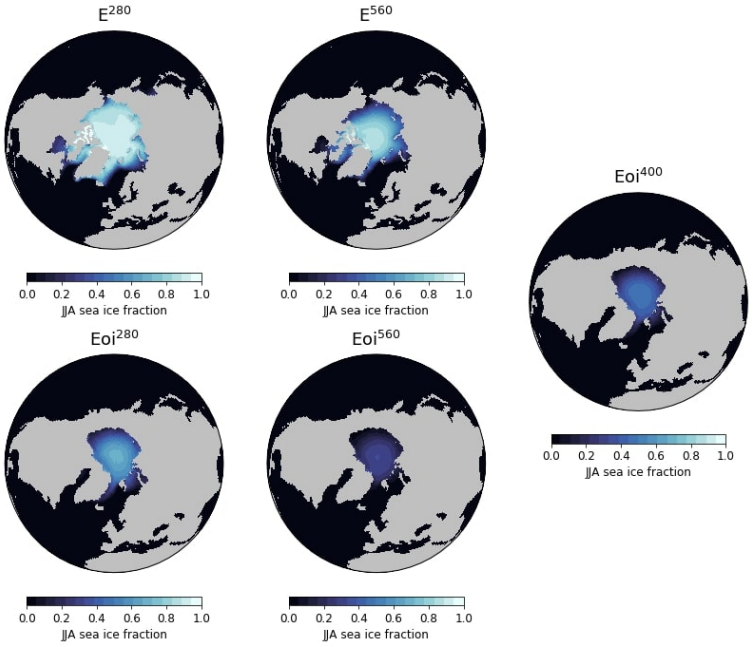

Supplementary Figure 2: Average simulated sea-ice fraction from June to August (JJA) for each simulation.

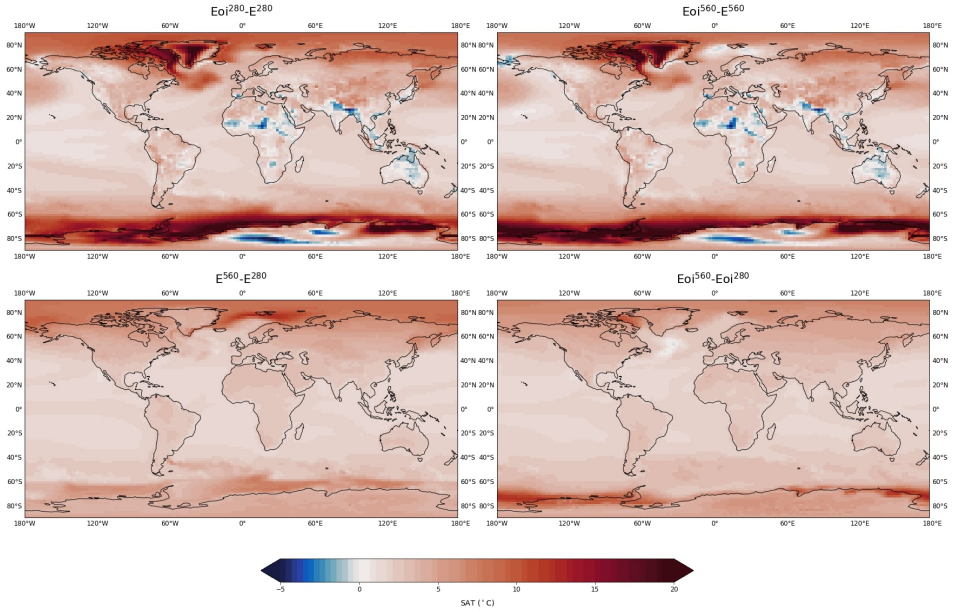

Supplementary Figure 3: Differences in average simulated surface air temperature.

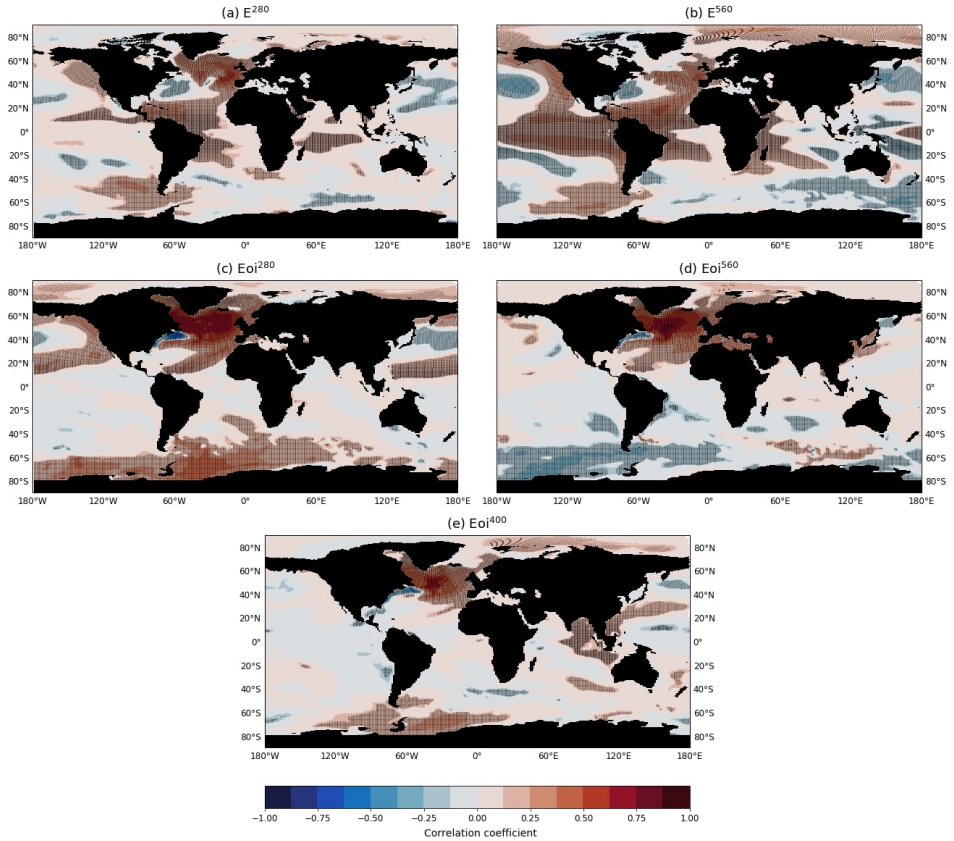

Supplementary Figure 4: Correlation between the SST and AMOC strength at each grid point with shading in areas where the correlation is above the 95% confidence level.

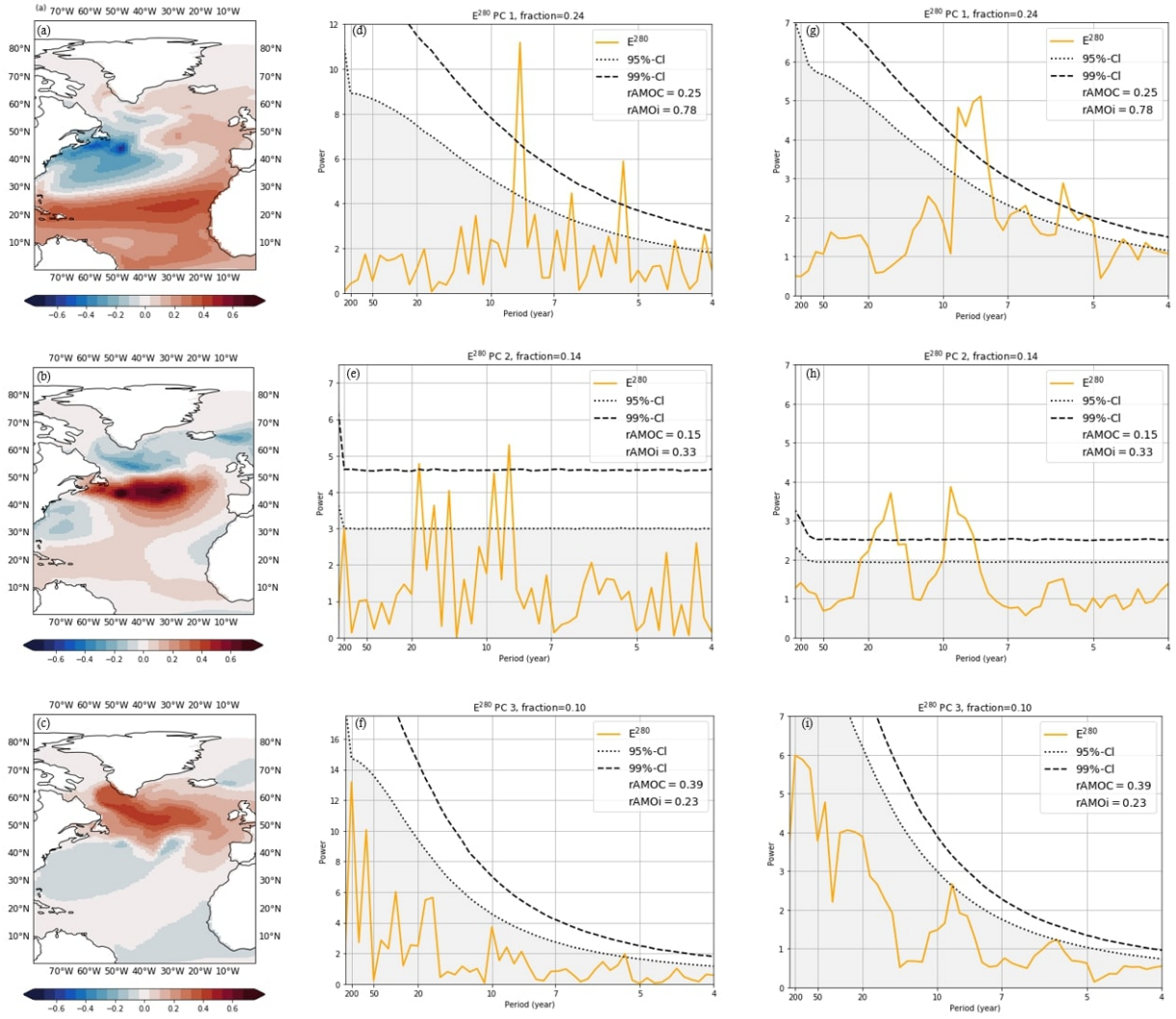

Supplementary Figure 5: (a) - (c): Three leading EOFs of E^{280}. (d) - (f): Fourier power spectra of the three leading standardized PCs of E^{280}. (g) - (i): MTM power spectra of of the three leading standardized PCs of E^{280}. The correlation between the PCs and the AMOC strength and AMO index is shown in the legend of each individual PC spectrum. The dotted line and shading indicates the 95% confidence level and the dashed line indicates the 99% confidence level, both using red noise as the null hypothesis.

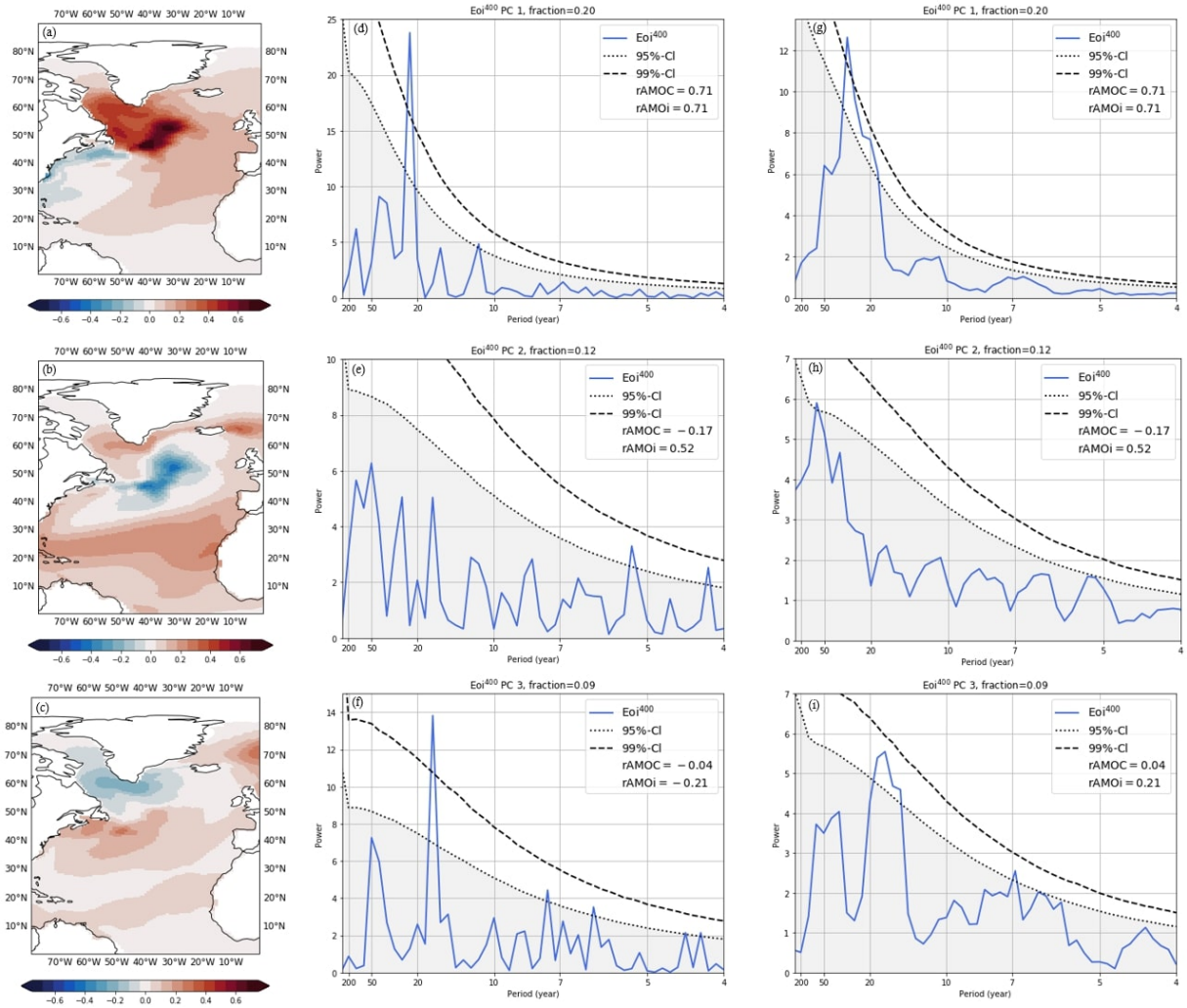

Supplementary Figure 6: (a) - (c): Three leading EOFs of Eoi^{400}. (d) - (f): Fourier power spectra of the three leading standardized PCs of Eoi^{400}. (g) - (i): MTM power spectra of of the three leading standardized PCs of Eoi^{400}. The correlation between the PCs and the AMOC strength and AMO index is shown in the legend of each individual PC spectrum. The dotted line and shading indicates the 95% confidence level and the dashed line indicates the 99% confidence level, both using red noise as the null hypothesis.

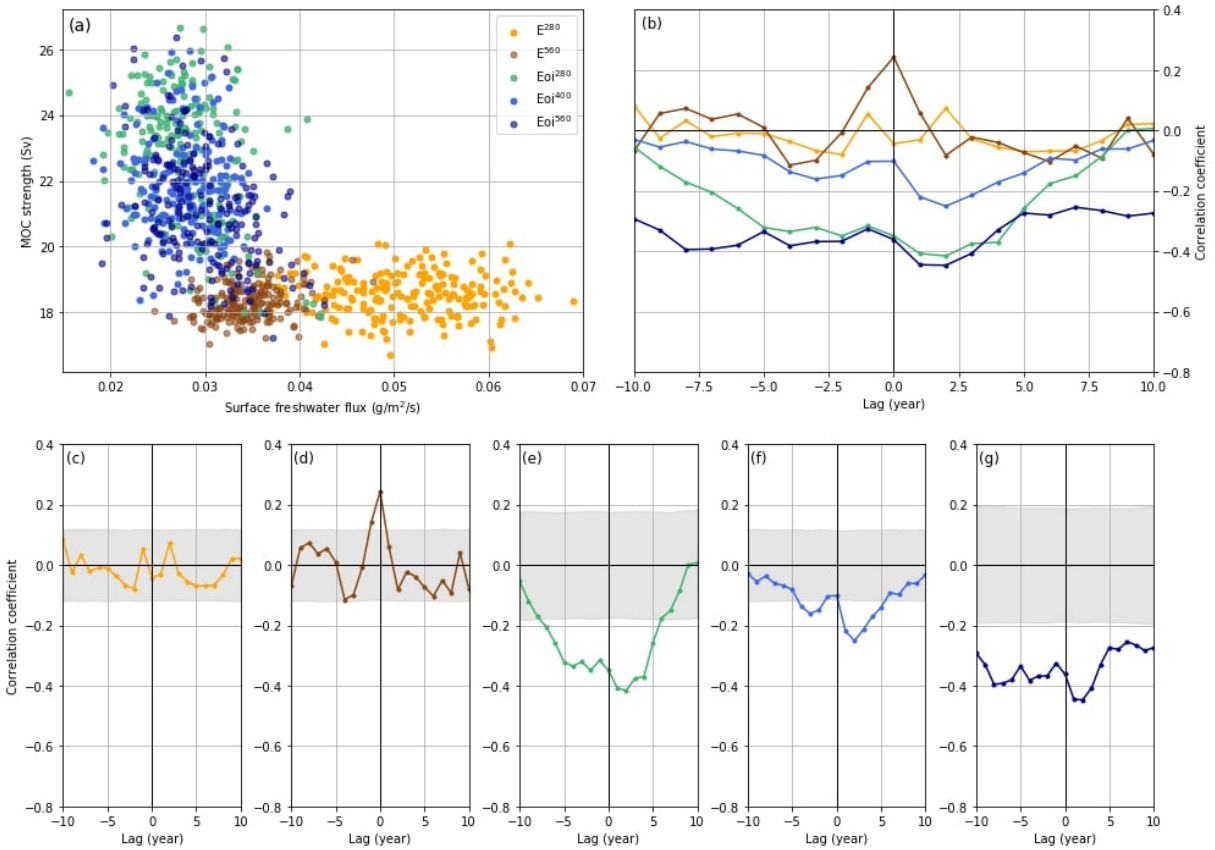

Supplementary Figure 7: (a): Yearly AMOC strength plotted against the yearly average surface freshwater flux in the Labrador Sea. (b): Correlation coefficients for each simulation between the yearly AMOC strength and Labrador Sea freshwater flux where a positive lag means the surface freshwater flux leads the AMOC. (c) - (g): Individual correlation coefficients for E^{280}, E^{560}, Eoi^{280}, Eoi^{400} and E^{560}, respectively. Shading indicates the 95% confidence interval using red noise as the null hypothesis.

References

Bryan, F. (1987). Parameter Sensitivity of Primitive Equation Ocean General Circulation Models. *Journal of Physical Oceanography*, 17(7):970–985. Publisher: American Meteorological Society Section: Journal of Physical Oceanography.

Burke, K. D., Williams, J. W., Chandler, M. A., Haywood, A. M., Lunt, D. J., and Otto-Bliesner, B. L. (2018). Pliocene and Eocene provide best analogs for near-future climates. *Proceedings of the National Academy of Sciences*, 115(52):13288–13293.

Caesar, L., Rahmstorf, S., Robinson, A., Feulner, G., and Saba, V. (2018). Observed fingerprint of a weakening Atlantic Ocean overturning circulation. *Nature*, 556(7700):191–196.

Delworth, T. L. and Zeng, F. (2012). Multicentennial variability of the Atlantic meridional overturning circulation and its climatic influence in a 4000 year simulation of the GFDL CM2.1 climate model. *Geophysical Research Letters*, 39(13). _eprint: https://agupubs.onlinelibrary.wiley.com/doi/pdf/10.1029/2012GL052107.

Dijkstra, H. A. (2007). Characterization of the multiple equilibria regime in a global ocean model. *Tellus A: Dynamic Meteorology and Oceanography*, 59(5):695–705. Publisher: Taylor & Francis _eprint: https://doi.org/10.1111/j.1600-0870.2007.00267.x.

Dolan, A. M., Hunter, S. J., Hill, D. J., Haywood, A. M., Koenig, S. J., Otto-Bliesner, B. L., Abe-Ouchi, A., Bragg, F., Chan, W.-L., Chandler, M. A., Contoux, C., Jost, A., Kamae, Y., Lohmann, G., Lunt, D. J., Ramstein, G., Rosenbloom, N. A., Sohl, L., Stepanek, C., Ueda, H., Yan, Q., and Zhang, Z. (2015). Using results from the PlioMIP ensemble to investigate the Greenland Ice Sheet during the mid-Pliocene Warm Period. *Climate of the Past Discussions*, 11(3):403.

Dowsett, H., Dolan, A., Rowley, D., Pound, M., Salzmann, U., Robinson, M., Chandler, M., Foley, K., and Haywood, A. (2016). The PRISM4 (mid-Piacenzian) palaeoenvironmental reconstruction. preprint, Proxy Use-Development-Validation/Marine Archives/Cenozoic.

Dowsett, H., Robinson, M., Haywood, A. M., Salzmann, U., Hill, D., Sohl, L. E., Chandler, M., Williams, M., Foley, K., and Stoll, D. K. (2010). The PRISM3D paleoenvironmental reconstruction. *Stratigraphy*, 7(2-3):123–139. Number: 2-3 Publisher: Micropaleontology Press.

Dowsett, H. J. (2007). The PRISM palaeoclimate reconstruction and Pliocene sea-surface temperature. *Deep-time perspectives on climate change: marrying the signal from computer models and biological proxies*, pages 459–480. Publisher: The Geological Society London.

Dowsett, H. J., Foley, K. M., Stoll, D. K., Chandler, M. A., Sohl, L. E., Bentsen, M., Otto-Bliesner, B. L., Bragg, F. J., Chan, W.-L., Contoux, C., Dolan, A. M., Haywood, A. M., Jonas, J. A., Jost, A., Kamae, Y., Lohmann, G., Lunt, D. J., Nisancioglu, K. H., Abe-Ouchi, A., Ramstein, G., Riesselman, C. R., Robinson, M. M., Rosenbloom, N. A., Salzmann, U., Stepanek, C., Strother, S. L., Ueda, H., Yan, Q., and Zhang, Z. (2013). Sea Surface Temperature of the mid-Piacenzian Ocean: A Data-Model Comparison. *Scientific Reports*, 3(1):2013.

Drijfhout, S., van Oldenborgh, G. J., and Cimatoribus, A. (2012). Is a Decline of AMOC Causing the Warming Hole above the North Atlantic in Observed and Modeled Warming Patterns? *Journal of Climate*, 25(24):8373–8379.

Frankcombe, L. M., von der Heydt, A., and Dijkstra, H. A. (2010). North Atlantic Multidecadal Climate Variability: An Investigation of Dominant Time Scales and Processes. *Journal of Climate*, 23(13):3626–3638. Publisher: American Meteorological Society.

Frenz, M., Henrich, R., and Zychla, B. (2006). Carbonate preservation patterns at the Ceará Rise – Evidence for the Pliocene super conveyor. *Marine Geology*, 232(3-4):173–180.

Haywood, A., Dowsett, H., Dolan, A., Rowley, D., Abe-Ouchi, A., Otto-Bliesner, B., Chandler, M., Hunter, S., Lunt, D., Pound, M., and Salzmann, U. (2016). The Pliocene Model Intercomparison Project (PlioMIP) Phase 2: scientific objectives and experimental design. *Climate of the Past*, 12(3):663–675. Number: 3 Publisher: Copernicus.

Haywood, A. M., Dowsett, H. J., Otto-Bliesner, B., Chandler, M. A., Dolan, A. M., Hill, D. J., Lunt, D. J., Robinson, M. M., Rosenbloom, N., Salzmann, U., and Sohl, L. E. (2010). Pliocene Model Intercomparison Project (PlioMIP): experimental design and boundary conditions (Experiment 1). *Geoscientific Model Development*, 3(1):227–242.

Haywood, A. M., Dowsett, H. J., Robinson, M. M., Stoll, D. K., Dolan, A. M., Lunt, D. J., Otto-Bliesner, B., and Chandler, M. A. (2011). Pliocene Model Intercomparison Project (PlioMIP): experimental design and boundary conditions (Experiment 2). *Geoscientific Model Development*, 4(3):571–577.

Haywood, A. M., Hill, D. J., Dolan, A. M., Otto-Bliesner, B. L., Bragg, F., Chan, W.-L., Chandler, M. A., Contoux, C., Dowsett, H. J., Jost, A., Kamae, Y., Lohmann, G., Lunt, D. J., Abe-Ouchi, A., Pickering, S. J., Ramstein, G., Rosenbloom, N. A., Salzmann, U., Sohl, L., Stepanek, C., Ueda, H., Yan, Q., and Zhang, Z. (2013). Large-scale features of Pliocene climate: results from the Pliocene Model Intercomparison Project. *Climate of the Past*, 9(1):191–209.

Haywood, A. M., Tindall, J. C., Dowsett, H. J., Dolan, A. M., Foley, K. M., Hunter, S. J., Hill, D. J., Chan, W.-L., Abe-Ouchi, A., Stepanek, C., Lohmann, G., Chandan, D., Peltier, W. R., Tan, N., Contoux, C., Ramstein, G., Li, X., Zhang, Z., Guo, C., Nisancioglu, K. H., Zhang, Q., Li, Q., Kamae, Y., Chandler, M. A., Sohl, L. E., Otto-Bliesner, B. L., Feng, R., Brady, E. C., Von der Heydt, A. S., Baatsen, M. L. J., and Lunt, D. J. (2020). A return to large-scale features of Pliocene climate: the Pliocene Model Intercomparison Project Phase 2. *Climate of the Past*. Publisher: European Geosciences Union.

Hurrell, J. W., Holland, M. M., Gent, P. R., Ghan, S., Kay, J. E., Kushner, P. J., Lamarque, J.-F., Large, W. G., Lawrence, D., Lindsay, K., Lipscomb, W. H., Long, M. C., Mahowald, N., Marsh, D. R., Neale, R. B., Rasch, P., Vavrus, S., Vertenstein, M., Bader, D., Collins, W. D., Hack, J. J., Kiehl, J., and Marshall, S. (2013). The Community Earth System Model: A Framework for Collaborative Research. *Bulletin of the American Meteorological Society*, 94(9):1339–1360. Publisher: American Meteorological Society Section: Bulletin of the American Meteorological Society.

Jackson, L. C., Kahana, R., Graham, T., Ringer, M. A., Woollings, T., Mecking, J. V., and Wood, R. A. (2015). Global and European climate impacts of a slowdown of the AMOC in a high resolution GCM. *Climate Dynamics*, 45(11-12):3299–3316.

Jayne, S. R. (2009). The Impact of Abyssal Mixing Parameterizations in an Ocean General Circulation Model. *Journal of Physical Oceanography*, 39(7):1756–1775. Publisher: American Meteorological Society.

Jochum, M. (2009). Impact of latitudinal variations in vertical diffusivity on climate simulations. *Journal of Geophysical Research: Oceans*, 114(C1). _eprint: https://onlinelibrary.wiley.com/doi/pdf/10.1029/2008JC005030.

Jüling, A., von der Heydt, A., and Dijkstra, H. A. (2020). Effects of strongly eddying oceans on multidecadal climate variability in the Community Earth System Model. *Ocean Science Discussions*, pages 1–24. Publisher: Copernicus GmbH.

Kanzow, T., Cunningham, S. A., Johns, W. E., Hirschi, J. J.-M., Marotzke, J., Baringer, M. O., Meinen, C. S., Chidichimo, M. P., Atkinson, C., Beal, L. M., Bryden, H. L., and Collins, J. (2010). Seasonal Variability of the Atlantic Meridional Overturning Circulation at 26.5°N. *Journal of Climate*, 23(21):5678–5698. Publisher: American Meteorological Society Section: Journal of Climate.

Koenig, S. J., Dolan, A. M., de Boer, B., Stone, E. J., Hill, D. J., DeConto, R. M., Abe-Ouchi, A., Lunt, D. J., Pollard, D., Quiquet, A., Saito, F., Savage, J., and van de Wal, R. (2015). Ice sheet model dependency of the simulated Greenland Ice Sheet in the mid-Pliocene. *Climate of the Past*, 11(3):369–381. Number: 3 Publisher: European Geosciences Union.

Kushnir, Y. (1994). Interdecadal Variations in North Atlantic Sea Surface Temperature and Associated Atmospheric Conditions. *Journal of Climate*, 7(1):141–157. Publisher: American Meteorological Society.

Large, W. G., McWilliams, J. C., and Doney, S. C. (1994). Oceanic vertical mixing: A review and a model with a nonlocal boundary layer parameterization. *Reviews of Geophysics*, 32(4):363–403. _eprint: https://agupubs.onlinelibrary.wiley.com/doi/pdf/10.1029/94RG01872.

Naish, T., Powell, R., Levy, R., Wilson, G., Scherer, R., Talarico, F., Krissek, L., Niessen, F., Pompilio, M., Wilson, T., Carter, L., DeConto, R., Huybers, P., McKay, R., Pollard, D., Ross, J., Winter, D., Barrett, P., Browne, G., Cody, R., Cowan, E., Crampton, J., Dunbar, G., Dunbar, N., Florindo, F., Gebhardt, C., Graham, I., Hannah, M., Hansaraj, D., Harwood, D., Helling, D., Henrys, S., Hinnov, L., Kuhn, G., Kyle, P., Läufer, A., Maffioli, P., Magens, D., Mandernack, K., McIntosh, W., Millan, C., Morin, R., Ohneiser, C., Paulsen, T., Persico, D., Raine, I., Reed, J., Riesselman, C., Sagnotti, L., Schmitt, D., Sjunneskog, C., Strong, P., Taviani, M., Vogel, S., Wilch, T., and Williams, T. (2009). Obliquity-paced Pliocene West Antarctic ice sheet oscillations. *Nature*, 458(7236):322–328. Number: 7236 Publisher: Nature Publishing Group.

Otto-Bliesner, B. L., Jahn, A., Feng, R., Brady, E. C., Hu, A., and Löfverström, M. (2017). Amplified North Atlantic warming in the late Pliocene by changes in Arctic gateways. *Geophysical Research Letters*, 44(2):957–964.

Pagani, M., Liu, Z., LaRiviere, J., and Ravelo, A. C. (2010). High Earth-system climate sensitivity determined from Pliocene carbon dioxide concentrations. *Nature Geoscience*, 3(1):27–30.

Percival, D. B., Walden, A. T., and others (1993). *Spectral analysis for physical applications*. cambridge university press.

Pollard, D. and DeConto, R. M. (2009). Modelling West Antarctic ice sheet growth and collapse through the past five million years. *Nature*, 458(7236):329–332. Publisher: Springer Nature.

Pound, M. J., Tindall, J., Pickering, S. J., Haywood, A. M., Dowsett, H. J., and Salzmann, U. (2014). Late Pliocene lakes and soils: a global data set for the analysis of climate feedbacks in a warmer world. *Climate of the Past*, 10(1):167–180. Publisher: Copernicus GmbH.

Ravelo, A. C. and Andreasen, D. H. (2000). Enhanced circulation during a warm period. *Geophysical Research Letters*, 27(7):1001–1004. _eprint: https://agupubs.onlinelibrary.wiley.com/doi/pdf/10.1029/1999GL007000.

Raymo, M., Grant, B., Horowitz, M., and Rau, G. (1996). Mid-Pliocene warmth: stronger greenhouse and stronger conveyor. *Marine Micropaleontology*, 27(1-4):313–326.

Smith, R., Jones, P., Briegleb, B., Bryan, F., Danabasoglu, G., Dennis, J., Dukowicz, J., Eden, C., Fox-Kemper, B., Gent, P., and others (2010). The parallel ocean program (POP) reference manual: ocean component of the community climate system model (CCSM) and community earth system model (CESM). *LAUR-01853*, 141:1–140.

Stepanek, C., Samakinwa, E., Knorr, G., and Lohmann, G. (2020). Contribution of the coupled atmosphere–ocean–sea ice–vegetation model COSMOS to the PlioMIP2. *Climate of the Past*, 16(6):2275–2323. Publisher: Copernicus GmbH.

Thomson, D. J. (1995). The seasons, global temperature, and precession. *Science*, 268(5207):59–68. Publisher: American Association for the Advancement of Science.

Thornalley, D. J. R., Oppo, D. W., Ortega, P., Robson, J. I., Brierley, C. M., Davis, R., Hall, I. R., Moffa-Sanchez, P., Rose, N. L., Spooner, P. T., Yashayaev, I., and Keigwin, L. D. (2018). Anomalously weak Labrador Sea convection and Atlantic overturning during the past 150 years. *Nature*, 556(7700):227–230.

Vallis, G. K. (2017). The Meridional Overturning Circulation and the acc. In *Atmospheric and Oceanic Fluid Dynamics: Fundamentals and Large-Scale Circulation*, pages 801–860. Cambridge University Press, 2 edition.

Vallis, G. K. and Farneti, R. (2009). Meridional energy transport in the coupled atmosphere-ocean system: scaling and numerical experiments: MERIDIONAL ENERGY TRANSPORT. *Quarterly Journal of the Royal Meteorological Society*, 135(644):1643–1660.

Viebahn, J. P., von der Heydt, A. S., Le Bars, D., and Dijkstra, H. A. (2016). Effects of Drake Passage on a strongly eddying global ocean. *Paleoceanography*, 31(5):564–581.

von der Heydt, A. S., Ashwin, P., Camp, C. D., Crucifix, M., Dijkstra, H. A., Ditlevsen, P., and Lenton, T. M. (2020). Quantification and interpretation of the climate variability record. preprint, EarthArXiv.

Yang, H., Li, Q., Wang, K., Sun, Y., and Sun, D. (2015). Decomposing the meridional heat transport in the climate system. *Climate Dynamics*, 44(9):2751–2768.

Zhang, Z., Li, X., Guo, C., Otterå, O. H., Nisancioglu, K. H., Tan, N., Contoux, C., Ramstein, G., Feng, R., Otto-Bliesner, B. L., Brady, E., Chandan, D., Peltier, W. R., Baatsen, M.

L. J., von der Heydt, A. S., Weiffenbach, J. E., Stepanek, C., Lohmann, G., Zhang, Q., Li, Q., Chandler, M. A., Sohl, L. E., Haywood, A. M., Hunter, S. J., Tindall, J. C., Williams, C., Lunt, D. J., Chan, W.-L., and Abe-Ouchi, A. (2021). Mid-Pliocene Atlantic Meridional Overturning Circulation simulated in PlioMIP2. *Climate of the Past*, 17(1):529–543.

Zhang, Z.-S., Nisancioglu, K. H., Chandler, M. A., Haywood, A. M., Otto-Bliesner, B. L., Ramstein, G., Stepanek, C., Abe-Ouchi, A., Chan, W.-L., Bragg, F. J., Contoux, C., Dolan, A. M., Hill, D. J., Jost, A., Kamae, Y., Lohmann, G., Lunt, D. J., Rosenbloom, N. A., Sohl, L. E., and Ueda, H. (2013). Mid-pliocene Atlantic Meridional Overturning Circulation not unlike modern. *Climate of the Past*, 9(4):1495–1504.